

**Target formation pore-pressure prediction using 3D seismic data
via the Fillippone and Eaton approaches in southern Sichuan,
China**

A Thesis Presented

to the Faculty of the Department of Earth and Atmospheric Sciences

University of Houston

In Partial Fulfillment

of the Requirements for the Degree

Master of Science

By

Zi Wang

May 2014

**Target formation pore-pressure prediction using 3D seismic data
via the Fillippone and Eaton approaches in southern Sichuan,
China**

Zi Wang

APPROVED:

Dr. Hua-Wei Zhou, Chairman

Dr. Aibing Li

**Dr. Jin Zhang, Ocean University of
China**

**Dean, College of Natural Sciences
and Mathematics**

Acknowledgements

My special thanks go to BGP Inc., China National Petroleum Corporation, for sharing geophysical data in southern Sichuan, China, and for permitting me to pursue this research in their laboratory. I would also like to thank Dr. Hua-wei Zhou, Rui Guo, Pei-ming Li, and Yu-sheng Zhang, for their technical assistance and suggestions, without which this project would never have reached fruition. Last, but certainly not least; my deepest gratitude goes to my parents for their constant encouragement and total support in my attainment of this goal.

**Target formation pore-pressure prediction using 3D seismic data
via the Fillippone and Eaton approaches in southern Sichuan,
China**

An Abstract of a Thesis

Presented to

the Faculty of the Department of Earth and Atmospheric Sciences

University of Houston

In Partial Fulfillment

of the Requirements for the Degree

Master of Science

By

Zi Wang

May 2014

Abstract

Abnormal pore pressure is a common occurrence in hydrocarbon basins due to hydrocarbon generation, migration, and accumulation. The study of changes in pore-pressure may reveal the enrichment characteristics and passageway of hydrocarbons, as well as lithological variation and characteristics. Abnormal pore pressure is directly related to the drilling safety and property security, and therefore important to oil and gas exploration. Such information will contribute toward a reasonable drilling fluid density design to ensure the stability of wellbore structure and the safety of drilling. In the southern Sichuan Basin, China, the potential shale gas formations usually have overpressure, so the ability to predict the pore pressure of the target formation is critical for shale gas exploration there and elsewhere. In this study, 36 square kilometers of 3D seismic data are used in testing several approaches of target formation pore-pressure prediction. In order to improve the velocity model, VSP data are used to correct acoustic velocity. Through the analysis and evaluation of pore-pressure prediction, a new approach of computing seismic velocity for normal compaction, called “Fillippone + Eaton” normal compaction velocity calculation, is introduced in this study based on the maximum and minimum compaction velocities calculated from the Fillippone formula. This new approach improves the inadequacy in the parameter setting of the two existing approaches. The feasibility of the new approach is verified through applying it using the 3D post-stack data in the study area, and the predicted pressure values match well with the measured pressure data.

Contents

1. Introduction	1
1.1 Motivation.....	1
1.2 Background of study area	2
1.3 Workflow	7
2. Study review.....	9
2.1 Introduction.....	9
2.2 Definitions.....	10
2.3 Abnormal pore-pressure.....	12
2.3.1 The origin of abnormal pressure	12
2.3.2 The basic principle of pore-pressure prediction.....	13
3. Methodology	16
3.1 Well-logging velocity corrections.....	16
3.1.1 VSP velocity	16
3.1.2 Well-logging velocity corrections.....	18
3.2 Density	21
3.3 D exponent.....	23

3.4	The Fillippone approach	24
3.4.1	The Fillippone approach Test 1	25
3.4.2	The Fillippone approach Test 2	30
3.4.3	The Fillippone approach Test 3	33
3.5	The Eaton approach	36
3.5.1	Basic principle	36
3.5.2	Test of the Eaton approach	39
3.5.3	The Fillippone + Eaton approach	43
3.5.3.1	The Fillippone + Eaton approach 1	43
3.5.3.2	The Fillippone + Eaton approach 2.....	45
4.	Pore-pressure prediction in the target formation.....	49
4.1	Model-based inversion.....	49
4.2	3D pore-pressure prediction in the target formation.....	50
5.	Conclusions	61
6.	Future work.....	64
7.	References	65

List of Figures

Figure 1.1 – The study area in the southern Sichuan Basin, China	3
Figure 1.2 – Workflow	8
Figure 2.1 – The relationship between overburden pressure and the pore-pressure....	12
Figure 3.1 – First-break picks of zero-offset downgoing P-wavefield for Well A	17
Figure 3.2 – Synthetic test of the zero-offset VSP velocity analysis for Well A acquisition geometry	18
Figure 3.3 – Comparison of the well-logging velocities with the VSP velocities (a) in depth domain, and (b) in time domain....	19
Figure 3.4 – Comparison of the corrected well-logging velocities with the VSP velocities (a) in depth domain, and (b) in time domain	21
Figure 3.5 – (a) Comparison of the density profile is estimated based on the Gardner formula, corrected Gardner formula, and the measurement in depth domain, and (b) overburden pressure estimated by the original and the corrected Gardner formulas in depth domain.....	22
Figure 3.6 – Comparison of the overburden, hydrostatic, and the D exponent pressure (a) in depth domain, and (b) in time domain.	24

Figure 3.7 – Comparison of the corrected well-logging velocities with the RMS velocities in time domain	27
Figure 3.8 – (a) RMS velocities based on different time intervals in time domain, and (b) V_{max} and V_{min} with corresponding time intervals in time domain.....	28
Figure 3.9 – (a) Comparison of the predicted pore-pressure of different time intervals in time domain, and (b) smoothed pressure curves in time domain	28
Figure 3.10 – (a) V_{max} , V_{min} , and V_{inst} are estimated based on the layer division of geological information in time domain, and (b) comparison of the predicted pore-pressure with the D exponent pressure in time domain.....	29
Figure 3.11 – (a) V_{max} , V_{min} , and V_{inst} are estimated based on the empirical parameters in depth domain, and (b) comparison of the predicted pore-pressure with the D exponent pressure in depth domain.....	31
Figure 3.12 – Comparison of the predicted pore pressure after slope corrections with the D exponent pressure in depth domain.....	32
Figure 3.13 – (a) V_{mxp} , V_{mnp} , and V_{inst} in time domain, and (b) comparison of the predicted pore-pressure with the D exponent pressure in time domain.....	34
Figure 3.14 – Comparison of the predicted pore-pressure after corrections with the D exponent pressure in time domain	35
Figure 3.15 – Hydrostatic pressure, pore pressure, overburden stress, and effective stress in a borehole.....	37
Figure 3.16 – (a) Comparison of the normal compaction velocities with the	

instantaneous velocities in depth domain, and (b) comparison of the predicted pore-pressure with the D exponent pressure in depth domain.....	39
Figure 3.17 – Comparison of the predicted pore pressures after slope corrections with the D exponent pressure in depth domain.....	40
Figure 3.18 – (a) Comparison of the normal compaction velocities with the instantaneous velocities in depth domain, and (b) comparison of the predicted pore pressure with the D exponent pressure in depth domain	41
Figure 3.19 – Comparison of the predicted pore pressures after slope corrections with the D exponent pressure in depth domain	42
Figure 3.20 – V_{mxp} , V_{mnp} , V_{normal} , and V_{inst} in time domain	44
Figure 3.21 – Comparison of the predicted pore pressure with the D exponent pressure in time domain	44
Figure 3.22 – Comparison of the predicted pore-pressure after slope corrections with the D exponent pressure in time domain.....	45
Figure 3.23 – Comparison of the normal compaction velocities based on two approaches in time domain	46
Figure 3.24 – Comparison of the predicted pore pressure based on the Fillippone + Eaton approach 2 with the D exponent pressure in time domain	47
Figure 3.25 – Comparison of the predicted pore pressure after slope corrections with the D exponent pressure in time domain.....	48
Figure 4.1 – Model-based inversion flowchart	50

Figure 4.2 – Initial model for velocity inversion in time domain.....	51
Figure 4.3 – Impedance inversion results in time domain	51
Figure 4.4 – Velocity inversion results in time domain	52
Figure 4.5 – Density inversion results in time domain	53
Figure 4.6 – (a) 3D pore-pressure prediction results, (b) inline, xline, and target formation 3D pore-pressure prediction results with Well A, (c) inline cross section profile with Well A, (d) xline cross section profile with Well A, and (e) target formation cross section profile with Well A	55
Figure 4.7 – (a) 3D pore-pressure prediction coefficient results, (b) inline, xline, and target formation 3D pore-pressure prediction results with Well A, (c) inline cross section profile with Well A, (d) xline cross section profile with Well A, and (e) target formation cross section profile with Well A	56
Figure 4.8 – Predicted pore-pressure in the target formation	57
Figure 4.9 – Predicted pore-pressure coefficient results in the target formation.....	58
Figure 4.10 – Velocity inversion results in the target formation.....	58
Figure 4.11– Comparison of the velocity inversion results with the well-logging velocity measurements for Well B in depth domain	59
Figure 4.12 – Comparison of the predicted pore-pressure coefficient results with the pressure coefficient measurements for Well B in depth domain.....	60

List of Tables

Table 1.1 – Stratigraphic column of the southern Sichuan Basin, China.....	4
Table 1.2 – Stratum data of Well A	5
Table 1.3 – Lithology of Well A.....	6
Table 1.4 – Stratum data of Well B	6

Chapter 1

Introduction

1.1 Motivation

The abnormal pore-pressure in potential hydrocarbon formation is a ubiquitous phenomenon in hydrocarbon-bearing basins. It is associated with the hydrocarbon generation, migration, and accumulation. In the southern Sichuan Basin, abnormally high-pressures often exist in potential shale gas formations, so appropriate pore-pressure prediction in the target layer before drilling can help determine the potential shale gas reservoir locations. As we know, abnormally high-pressure increases well risk, such as borehole influx or blow out. The prediction of abnormally high-pressure before drilling improves the drilling design and ensures the safety for both wells and workers.

Since only two wells exist in the study area, we can only analyze the given data to establish an easy-to-use pore-pressure prediction approach in this case to obtain a 3D pressure prediction field. The new easy-to-use pore-pressure prediction approach may help improve the pressure prediction by analyzing the relatively high or low pressure zones in the target layers. Therefore, the pore-pressure prediction results can be used

as a reference for potential shale gas reservoir prediction before drilling.

1.2 Background of study area

The Sichuan Basin is located at the western part of the Yangtze platform in southern China. This 180 thousand-square-kilometer basin was uplifted as the result of the Tong-wan tectonic movement at the end of the Sinian period. As one of the largest hydrocarbon-bearing basins in China, the Sichuan Basin has been explored for 60 years. The basin has 106 gas fields and 14 oil fields with proven reserves totaling 840 billion cubic meters of gas and 145 thousand tons of oil, respectively (Chen et al., 2011). The southern Sichuan Basin is one of the first strategic pilot test areas for shale gas exploration in China, and the Longmaxi Formation is one of the few mature shale gas formations in China. My study area covers about 150 square kilometers and is located nearly the margin of the basin (Figure 1.1).

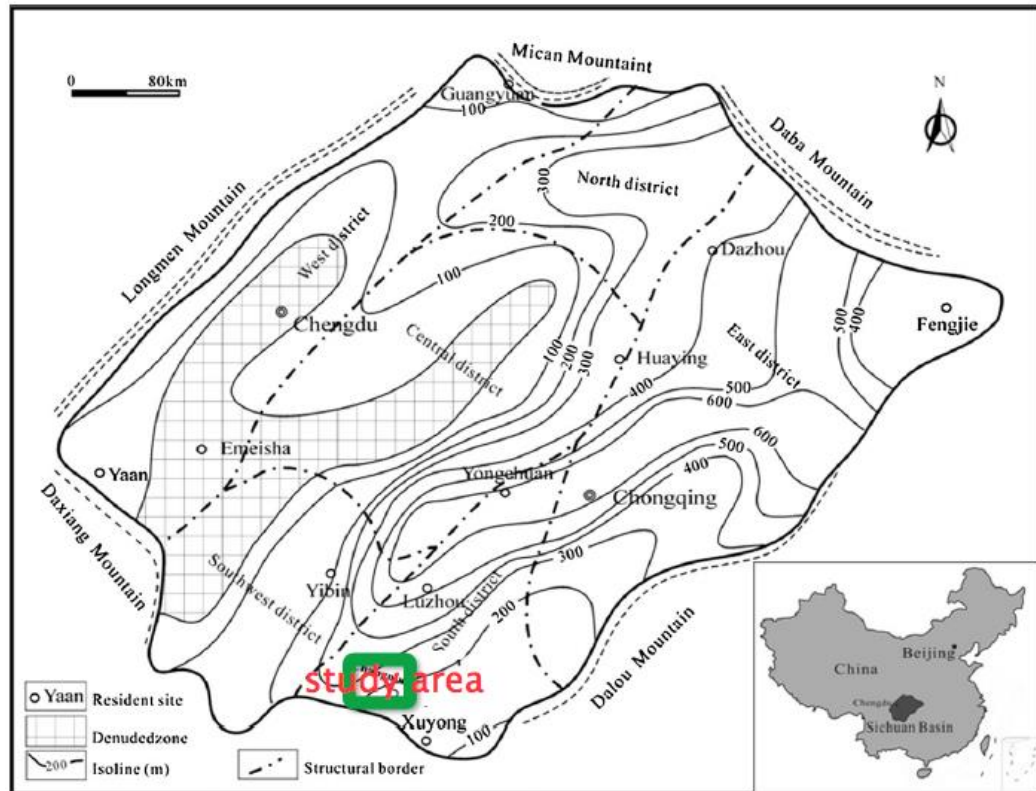




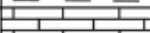









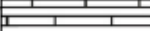

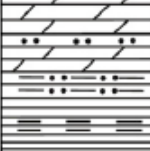








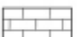





Figure 1.1 – The study area in the southern Sichuan Basin, China (Chen et al., 2011).

Table 1.1 shows the stratigraphic column of the southern Sichuan Basin. In the study area, the target geological formations are Longmaxi black shale as well as the Longmaxi Formation. The thickness of the Longmaxi Formation is based on depositional environment and subsequent erosional events related to its tectonic history. The lateral extent and thickness of the Longmaxi Formation is stable; its lithology consists of black shale, dark grey shale, and silty mudstone. The target formation has a high potential for gas production due to the high organic content, sapropelic quality, and high thermal maturity. The lower part of the Longmaxi Formation contains more than 50% quartz, which is the ideal composition for shale gas exploration and development (Chen et al., 2011).

Table 1.1 – Stratigraphic column of the southern Sichuan Basin, China (Chen et al., 2011).

System and Formation				Lithology	Thickness (m)	Source rock	Reservoir	
							Conventional	Shale gas
Mesozoic								
Paleozoic	Permian	Changxing	P _{1c}		200~500			
		Longtan	P _{1l}					
		Maokou	P _{1m}		200~500			
		Liangshan	P _{1l}					
	Carboniferous	Huanglong	C _{2h}		0~500			
	Silurian	Hanjiadian	S _{2h}		20~330			
		Shiniulan	S _{1s}		240~500			
		Longmaxi	S _{1l}		230~670			
	Ordovician	Wufeng	O _{2w}		320~960			
		Linxiang	O _{2l}					
		Baota	O _{2b}					
	Cambrian		Є		620~1330			
Proterozoic								

	Shale		Mudstone		Sandstone		Conglomerate		Conventional reservoir
	Coal		Limestone		Dolomite		Source rock		Shale gas reservoir

Up to now, only two wells have been drilled in study area, Well A and Well B. Well A is used as a testing well. The purpose is to test an appropriate pore-pressure prediction approach for 3D application. Well B is used as checking well to check the final pore-pressure prediction result with the pressure measurement. The geological information of Well A is shown in Table 1.2.

Table 1.2 – Stratum data of Well A.

Stratum				Drilling measurement	
System	Series	Formation	Mark	Bottom depth(m)	Thickness(m)
			Q	8	3
Triassic	Lower	Tongjiezi	T _{1t}	31	23
		Feixianguan	T _{1f}	561	530
Permian	Upper	Leping	P _{2l}	704	143
		Xuanwuyan	P _{2β}	824	120
	Lower	Maokou	P _{1m}	1081	257
		Qixia	P _{1q}	1344	263
		Liangshan	P _{1l}	1349	5
Silurian	Middle	Luoreping	S _{2l}	1859	510
	Lower	Longmaxi	S _{1l}	2055	194
Ordovician	Upper	Wufeng	O _{3w}	2066	10
	Middle	Baota	O _{2b}	2117	51

Well A is 2177 m deep. The Longmaxi Formation occurs from 1859 m to 2055 m depth (See Table 1.2).

According to the gamma ray logging and drilling data, there is a variety of lithologies in Well A (See Table 1.3). In the target formation, from 1850 m to 2050 m, the stratigraphy consists of shale.

Table 1.3 – Lithology of Well A.

Depth(m)	Lithology
0-350	Shale
350-550	Sandstone
550-700	Coal
700-1400	Basalt
1400-1550	Shale
1550-1850	Sandstone
1850-2050	Shale

The geological information of Well B is given in Table 1.4.

Table 1.4 – Stratum data of Well B.

Stratum				Drilling measurement	
System	Series	Formation	Mark	Bottom depth(m)	Thickness(m)
			Q	5	5
Triassic	Lower	Jialingjiang	T _{1j}	52	47
		Tongjiezi	T _{1t}	152	100
		Feixianguan	T _{1f}	680	528
Permian	Upper	Leping	P _{2l}	785	105
		Xuanwuyan	P _{2β}	882	97
	Lower	Maokou	P _{1m}	1259	377
		Qixia	P _{1q}	1386	127
		Liangshan	P _{1l}	1398	12
Silurian	Middle	Luoreping	S _{2l}	1957	559
	Lower	Longmaxi	S _{1l}	2183	226
Ordovician	Upper	Wufeng	O _{3w}	2191	8
	Middle	Baota	O _{2b}	2220	29

The bottom depth of Well B is 2220 m. The thickness of the Longmaxi Formation is 226 m, and its bottom depth is 2183 m (Table 1.4).

1.3 Workflow

To accomplish pore-pressure prediction in the study area, regional geological data, drilling data, well-logging data, and VSP data of Well A are used. The workflow is as follows (See Figure 1.2):

- Apply VSP velocity of Well A to correct logging velocity;
- Use the corrected logging velocity to calculate density, overburden pressure, and hydrostatic pressure;
- Test appropriate prediction approaches using D exponent pressure;
- Use the Eaton formula (based on the new normal compaction velocity calculation approach, called the Fillippone + Eaton approach);
- Establish velocity background based on corrected logging velocity and geological stratum data;
- Conduct the model-based inversion with seismic trace data;
- Convert impedance inversion results to velocity and density;
- Use velocity inversion result in the pore-pressure prediction;
- Compare the predicted pressure coefficients of Well B with measurement pressure coefficients to prove the usefulness of pressure prediction approach.

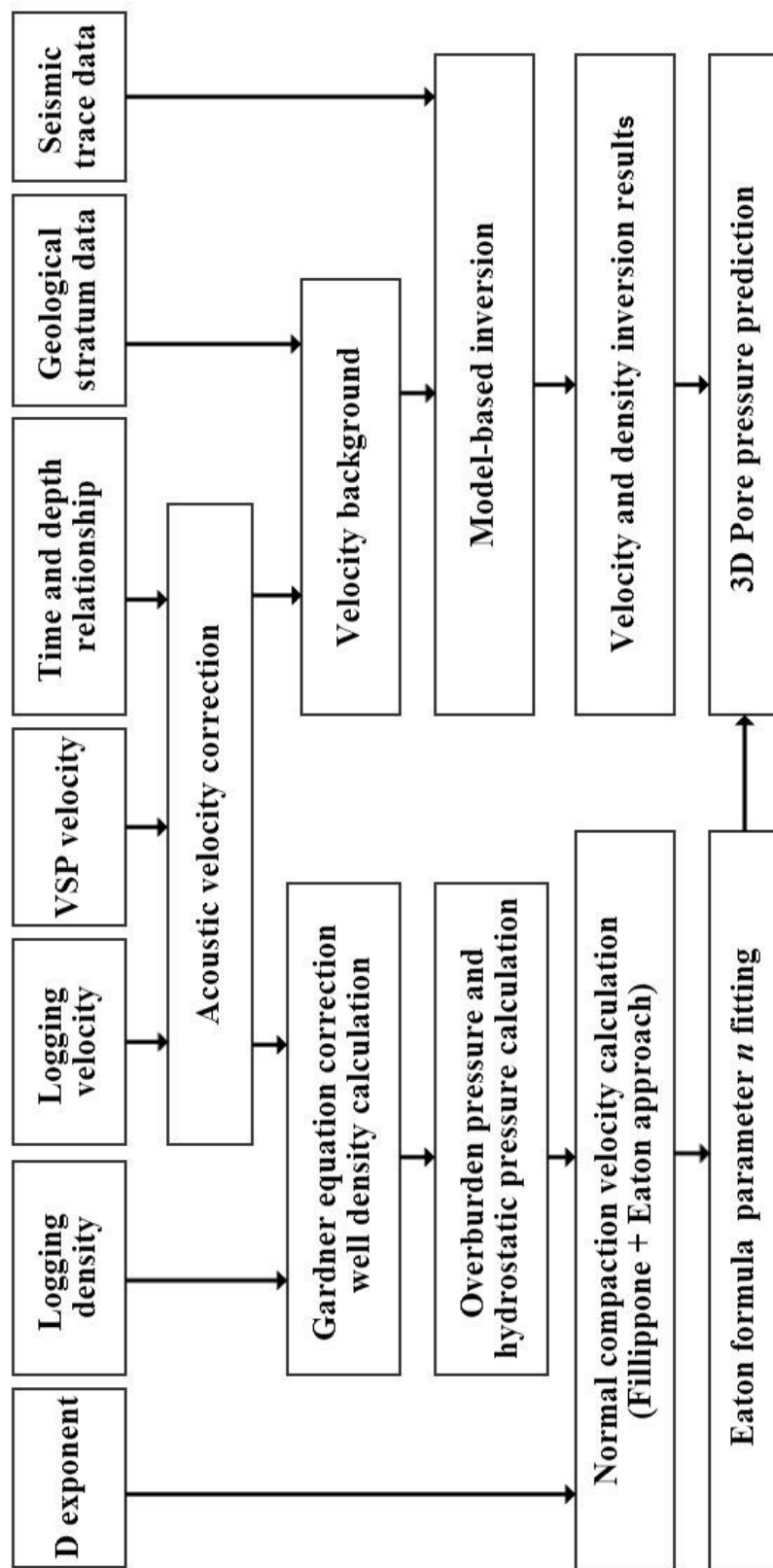


Figure 1.2 – Workflow.

Chapter 2

Study review

2.1 Introduction

Abnormal pressure is a subsurface situation in which the pore pressure of a geologic formation differs from the hydrostatic pressure. High formation pressures cause major changes in subsurface rock parameters. In the overpressured shale, seismic velocity and density are usually low, and the porosity is high. Detection of overpressured sediments can contribute to the overall analysis of a basin's hydrocarbon potential (Martinez et al., 1987). But overpressure in a formation can also result in dangerous well blowouts during drilling.

Overpressured formations exhibit several properties that differ from normal pressure formations, e.g. higher porosities, lower bulk densities, lower effective stress, higher temperatures, lower interval velocities, and higher Poisson's ratio.

2.2 Definitions

- Stress

Stress is defined as the internal forces that neighboring particles exert on each other at a point.

- Hydrostatic pressure

Hydrostatic pressure is defined as pressure exerted at the bottom of a water column or at a certain depth. It usually associated with following properties: (a) pressure increase with depth, and (b) pressure changes only depend on water density variation. Hydrostatic pressure can be determined using following formula (Chilingar et al., 2002):

$$P_{Hydrostatic} = \rho g h , \quad (2.1)$$

where, $P_{Hydrostatic}$ is hydrostatic pressure, h is the height of fluid column, ρ is liquid density, and g is the gravitational constant.

- Overburden pressure

Overburden pressure, also called lithostatic pressure, is the pressure imposed on a layer of soil or rock by the weight of overlying material. Overburden pressure can be determined by following formula (Chilingar et al., 2002):

$$P_{Overburden} = \int_0^h \rho (z) g dz , \quad (2.2)$$

where, $P_{Overburden}$ is overburden pressure, $\rho (z)$ is the density of overlying

rock at depth z , and g is gravitational acceleration.

- Formation pressure

Formation pressure is the pressure of fluids within the pores of a reservoir, usually presented by $P_p(z)$, i.e. pore-pressure. Formation pressure gradient is also called fluid pressure gradient, which refers to the value of fluid pressure per unit depth, and presented by G_p (Chilingar et al., 2002):

$$G_p(z) = \frac{P_p(z)}{z} . \quad (2.3)$$

Pressure gradient and pressure coefficients usually used to represent pore-pressure. The pressure coefficient indicates the difference between formation pressure and the normal pressure at the same point, and it can also present the ratio of formation pressure and hydrostatic pressure at the same point.

The formula is (Chilingar et al., 2002):

$$\alpha_p(z) = \frac{P_p(z)}{P_{Hydrostatic}(z)} . \quad (2.4)$$

- Effective stress

Effective stress is the stress imposed on the rock skeleton particles in the formation, which has a reversal relationship with pore-pressure (Figure 2.2). Its calculation depends on two parameters, namely, total stress and pore-pressure (Chilingar et al., 2002):

$$P_{overburden}(z) = \sigma(z) + P_f(z) . \quad (2.5)$$



Figure 2.1 – The relationship between overburden pressure and the pore-pressure

(Bowers, 2002).

- Sediment consolidation

The forces acting on a unit of sediment control its compaction. In nature, the load acting on a unit of sediment is carried by the (a) skeletal framework, and (b) the interstitial fluid in the pores (Chilingar et al., 2002).

2.3 Abnormal pore-pressure

2.3.1 The origin of abnormal pressure

Diverse factors can result in abnormal pore-pressure, such as physical factors, chemical factors, or a combination of them. Abnormal pore pressure includes abnormally low pore pressure and abnormally high pore pressure. Abnormally high pore-pressure distribution range is more common than that of the abnormally low pore-pressure; and abnormally high pore pressure has more harmful effects for drilling than the low pore pressure.

The origin of abnormally high pore pressure is complicated; several genetic mechanisms are responsible for the generation of abnormal pressure, as Swarbrick

and Osborne (1998) summarized:

- Stress- related (i.e. compression leading to pore-volume reduction)

Mechanism: Disequilibrium compaction (vertical loading stress),

Tectonic stress (lateral compressive stress).

- Increase in fluid volume

Mechanisms: Temperature increase (aquathermal),

Water release due to mineral transformation,

Hydrocarbon generation,

Cracking of oil to gas.

- Fluid movement and buoyancy

Mechanisms: Osmosis,

Hydraulic head,

Buoyancy due to density contrasts.

2.3.2 The basic principle of pore-pressure prediction

Five main factors are discussed in this chapter.

- Degree of sediment compaction

Normal pressure – normal degree of compaction,

Abnormally high pore-pressure – formation under compacted,

Abnormally low pore-pressure – formation over compacted.

The degree of sediment compaction in high-pressure formations is usually lower than that of normal-pressure formation. This results in the drilling rate abruptly increasing in the high-pressure transition zone during drilling.

- Permeability

An abnormally high-pressured formation has high fluid content, which can maintain its pore space and result in high porosity and permeability.

- Velocity

Velocity has a proportional relationship with degree of sediment compaction, and an inverse relationship with pressure.

An abnormally high-pressured formation has high porosity which results in low velocity. This is the basic principle for the pore-pressure prediction approaches based on the logging velocity data and seismic velocity data.

The relationship is:

Abnormally high-pressure – low velocity,

Abnormally low-pressure – high velocity.

- Density

Density has an inverse relationship with pressure.

An abnormally high-pressured formation has a low degree of sediment compaction, and results in low density value.

The relationship is:

Abnormally high-pressure – low density,

Abnormally low-pressure – high density.

- Resistivity

An abnormally high-pressured formation has high fluid content, which consists of high salinity values, hence a high conductivity value.

Conductivity has an inverse relationship with resistivity,

Abnormally high-pressure – low electrical resistivity,

Abnormally low-pressure – high electrical resistivity.

Chapter 3

Methodology

3.1 Well-logging velocity corrections

3.1.1 VSP velocity

The VSP velocity has the advantage in constructing the relationship between depth and time. So the VSP data is commonly used to correct well-logging velocity. Here the zero-offset VSP data processing steps are: first-break picks, flattening, velocity analysis, median filter (separation of upgoing and downgoing wavefields), deconvolution, NMO correction, and corridor stack.

In this study the interval analysis is conducted using the downgoing P-wavefield of Well A (information can be found in last section). Figure 3.1 shows the first-break picking results, where the green line indicates the first-break picks.

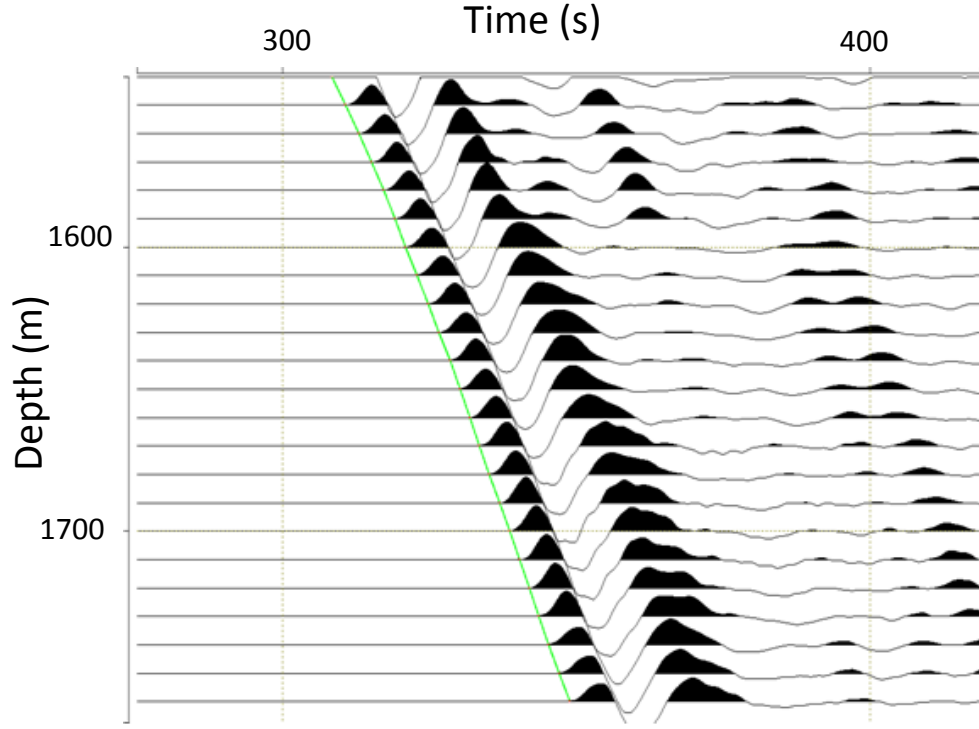


Figure 3.1 – First-break picks of zero-offset downgoing P-wavefield for Well A.

By calculating the slope of first-breaks for the downgoing P-wavefield, the interval velocity can be estimated. With the known geophone interval (10 m), the interval velocities (V_i , i stands for the i^{th} layer) can be obtained by dividing the depth interval Δz of the i^{th} layer by the differential travel time of the downgoing P-wave first-break picks, as shown in formula 3.1:

$$V_i = \frac{\Delta z}{t_i - t_{i-1}} . \quad (3.1)$$

Taking the corresponding values into formula 3.1, the velocity-depth relations can be estimated. Figure 3.2 shows a synthetic test of the effectiveness of formula 3.1.

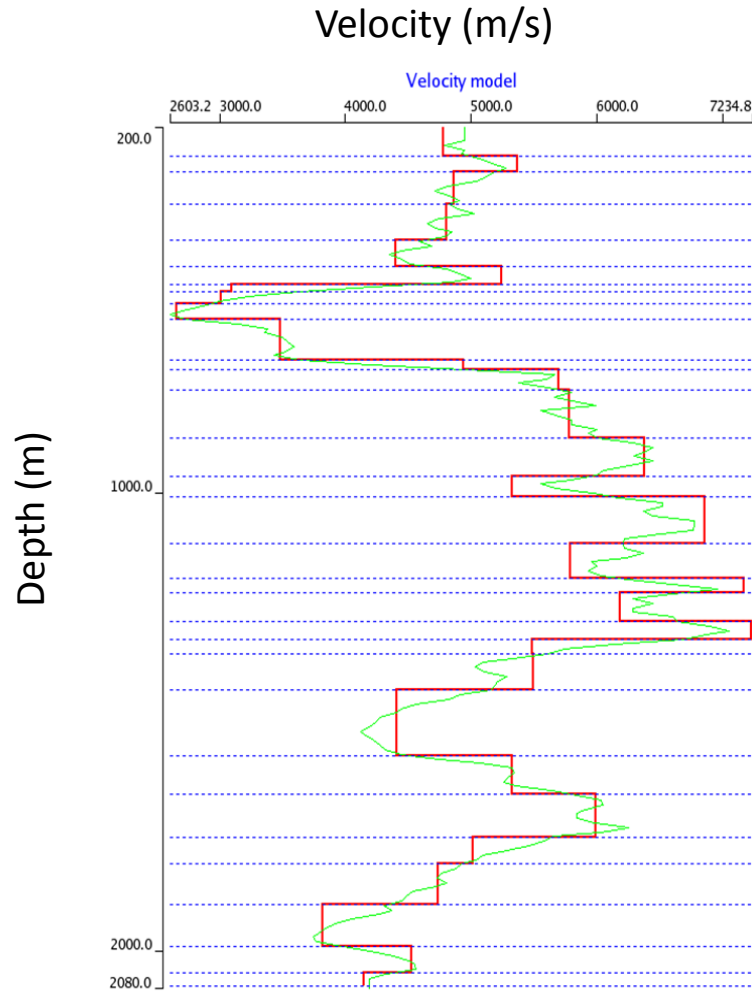


Figure 3.2 – Synthetic test of the zero-offset VSP velocity analysis for Well A acquisition geometry. The red line depicts the true interval velocities and the green line shows the velocities estimated by formula 3.1.

3.1.2 Well-logging velocity corrections

Acoustic well-logging are operated at frequency range around 5 – 10 kHz (Dutta, 2002), which is much higher than the frequency bandwidth of seismic data at 10 - 100 Hz. In other words, the resolution of velocity measurements based on well-logging

data is much higher than that based on the seismic data. Therefore, an appropriate calibration of the seismic velocity is necessary using the acoustic velocity. Figure 3.3 shows the comparison between the well-logging and the VSP velocities for Well A.

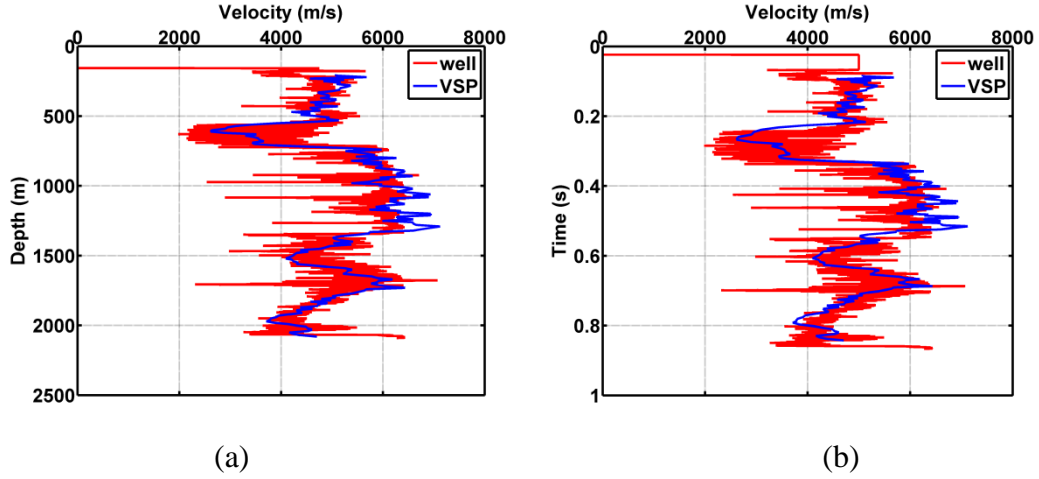


Figure 3.3 – Comparison of the well-logging velocities (red) with the VSP velocities (blue) (a) in depth domain, and (b) in time domain. Red and blue curves represent the well-logging velocities and the VSP velocities, respectively.

In the Figure 3.3 (b), the well-logging velocities has a time displacement compared with the VSP velocities in the target formation, which is from 0.75 s to 0.90 s. Since the well-logging velocity and the VSP velocity have sampling intervals at 0.15 m and 10 m, respectively, the first correction is to correct the sampling interval for those two velocity values into the same value:

$$\frac{0.15m}{V_{logging\ 1}} = t_1, \quad (3.2)$$

$$t_1 + t_2 + \dots + t_i = t_{total}, \quad (3.3)$$

$$\frac{10m}{t_{total}} = V_{logging\ average}, \quad (3.4)$$

$$V_{VSP} = a \times V_{logging\ average} + b, \quad (3.5)$$

where, $V_{logging\ 1}$ is the well-logging velocity with sampling interval at 0.15 m, t_i is the travel time of the downgoing P-wave first-break picks from the sampling interval at 0.15 m, t_{total} is the travel time of the downgoing P-wave first-break picks from the sampling interval at 10 m, $V_{logging\ average}$ is the well-logging velocity with sampling interval at 10 m, and V_{VSP} is the VSP velocity,

$$V_{after\ correction\ logging} = a \times V_{0.15m\ interval\ logging} + b, \quad (3.6)$$

where, $V_{after\ correction\ logging}$ is the well-logging velocity after corrections, $V_{0.15m\ interval\ logging}$ is the well-logging velocity with sampling interval at 0.15 m, a and b are correction parameters. The correction parameter a is 1.2258, and b is -535.1673.

Figure 3.4 (b) shows another comparison using the well-logging velocities after corrections, which has a good consistence with the VSP velocities. A reasonable matching with the VSP velocities is shown in the target formation from 0.75 s to 0.90 s. The well-logging velocities after corrections will be used to predict pore-pressure in later sections.

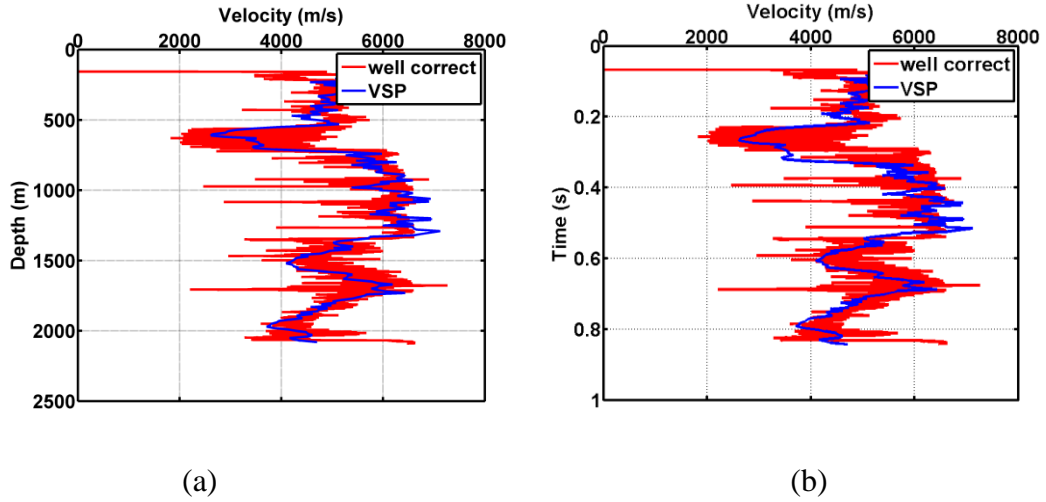


Figure 3.4 – Comparison of the corrected well-logging velocities (red) with the VSP velocities (blue) (a) in depth domain, and (b) in time domain.

3.2 Density

Density information is critical for evaluating overburden pressure, which is a key parameter in pore-pressure prediction. During well-logging, the density value is usually measured in some target depths. In Well A, density was measured from 1400 m to 2100 m. To estimate the density value in unmeasured depths, a conventional approach is based on the Gardner formula (Gardner et al., 1974):

$$\rho = A \times V^n, \quad (3.7)$$

where, V is the seismic velocity, A and n are the Gardner parameters. Typical A and n values are $A = 0.31$ and $n = 0.25$ in the Gulf Coast of Mexico (Gardner et al., 1974). As Gardner parameters are related to specific formation characteristics of the rock, it is necessary to estimate appropriate parameter values and establish a reasonable

formula correction based on the existing density data from the target region around Well A. According to the existing density data, the parameters are selected as $A = 1.60$, $n = 0.06$. Figure 3.5 (a) shows a comparison of density values estimated by different approaches.

By incorporating the density values estimated by the Gardner formula, the overburden pressure can be calculated by the formula 2.2.

Figure 3.5 (b) shows the overburden pressure estimated based on the Gardener density before and after corrections. Although there are significant difference in density distribution along depth after the corrections using the Gardner parameters in Figure 3.5 (a), the difference in the overburden pressure is small.

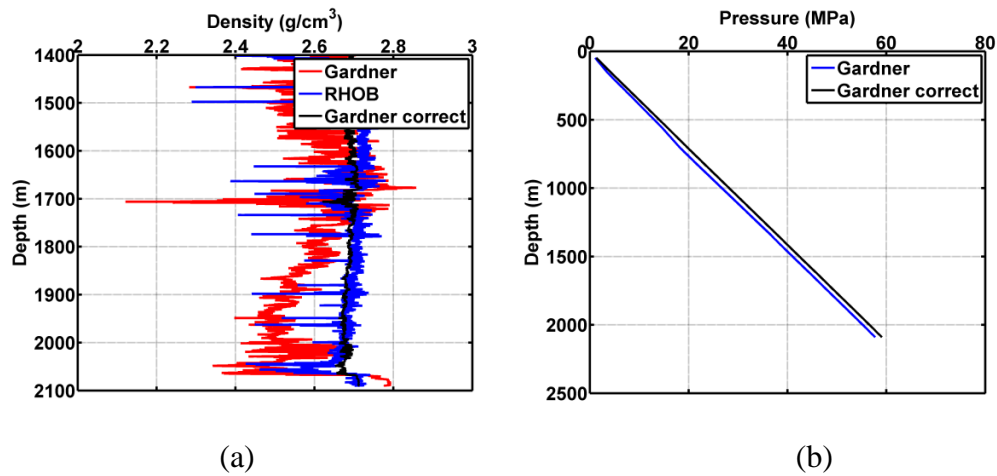


Figure 3.5 – (a) Comparison of the density profile is estimated based on the Gardner formula (red), corrected Gardner formula (black), and the measurement (blue) in depth domain, and (b) overburden pressure estimated by the original and the corrected Gardner formulas in depth domain.

3.3 D exponent (dcs)

In the normally compacted formation, with the increase of depth, the degree of compaction and rock density increase, while porosity and drilling rate decrease. Those changes lead to the increase of drilling time. Different from the drilling in the normal compaction zone, the drilling in the high-pressure transition zone will result in the increase of the drilling rate. To quantify the measurement of the drilling rate, the D exponent was proposed by Jorden and Shirley in 1966. In their approach the penetration rate was normalized based on drilling parameters. The D exponent reflects the formation “drillability” and removes the effects of weight on bit, drilling bit diameter, rotary speed, and other drilling factors. Under the same drilling conditions, the D exponent also implies the “drillability” of bit. In the normal compaction condition, the D exponent increases with depth; in the abnormally high-pressure transition zone, the D exponent value decreases with depth.

In this study, the pressure converted from the D exponent is used as the real pressure measurement to check the predicted pore-pressure at the same depth.

Figure 3.6 shows the overburden pressure (red), hydrostatic pressure (black), and the pressure converted from the D exponent (blue) in Well A. As seen in the figure, the D exponent pressure has extremely high values at certain depths which are likely artifact.

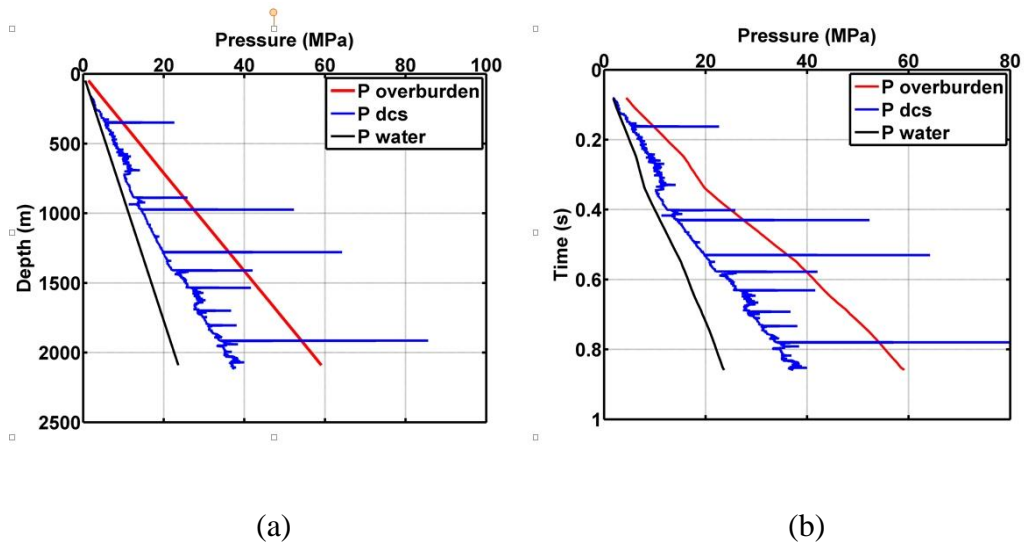


Figure 3.6 – Comparison of the overburden (red), hydrostatic (black), and the D exponent pressure (blue) (a) in depth domain, and (b) in time domain.

3.4 The Fillippone approach

The Fillippone approach depends upon the structural integrity of the rock, some proportional of the overburden load will be converted to pore-pressure. There are two extreme conditions. The first one is completely consolidated rock, in which case no overburden load converted to pore pressure. The second condition is unconsolidated rock or fluid-saturated shale, in which case a large percentage of the overburden load would be taken by the fluid in the pore space. Therefore the pore pressure is part of the overburden pressure. The Fillippone approach assumed this pressure proportions to the P-wave velocity of the rock (Martinez et al., 1987). Fillippone (1982) developed the following formula:

$$P_p = \frac{V_{p-grain} - V_{p-inst}}{V_{p-grain} - V_{p-fluid}} \times P_{overburden}, \quad (3.8)$$

where, P_p is the predicted pore-pressure, $V_{p-grain}$ is the P-wave velocity of rock with zero porosity (approximated to matrix velocity of the rock), $V_{p-fluid}$ is the P-wave velocity of rock with zero rigidity (approximated to pore fluid velocity), and V_{p-inst} is the instantaneous velocity (Chilingar et al., 2002).

In order to improve the accuracy of the pore-pressure prediction in the target formation, well-logging data, drilling data, density data, and VSP data were integrated to establish the appropriate velocity calculation.

3.4.1 The Fillippone approach Test 1

In the Fillippone approach, the $V_{p-grain}$ (V_{max}) and $V_{p-fluid}$ (V_{min}) are calculated in the following formulas (Fillippone, 1982):

$$\begin{cases} V_{max} = 1.4V_0 + 3KT \\ V_{min} = 0.7V_0 + 0.5KT \end{cases}, \quad (3.9)$$

where,

$$K = \frac{(V_Q - V_{Q_0})}{T_Q - T_{Q_0}}, \quad (3.10)$$

which is a velocity gradient with time, T_Q and T_{Q_0} are two-way travel time between the bottom and the top of a formation interval, V_Q and V_{Q_0} are the RMS velocities at time T_Q and T_{Q_0} , $T = T_Q$, and

$$V_0 = V_Q - KT_Q. \quad (3.11)$$

The Fillippone approach is based on the interpolation of seismic velocity between

two extreme conditions, i.e. no-porous solid and pure fluid.

The Fillippone formula has several assumptions when applying to real data. Four assumptions are taken for the approach (Fillippone, 1979):

- (1) The product of time and RMS velocity must be increase with the increase of travel times;
- (2) The interval velocity must be neither lower than 1371 m/s nor greater than 5273 m/s for sandstones and shale, and 6949 m/s for carbonates;
- (3) Times must increase in sequential order, while velocities usually increase in sequential order for common time values;
- (4) The time interval between accepted pairs should not be less than 50 millisecond of reflection time.

The RMS velocity calculation is based on well-logging velocity after corrections. Figure 3.7 shows the velocities inverse from 0.3 s to 0.4 s. The RMS reversal phenomenon conflicts with the first assumptions in the Fillippone approach, so the reasonable time interval stratification is used to solve this conflict.

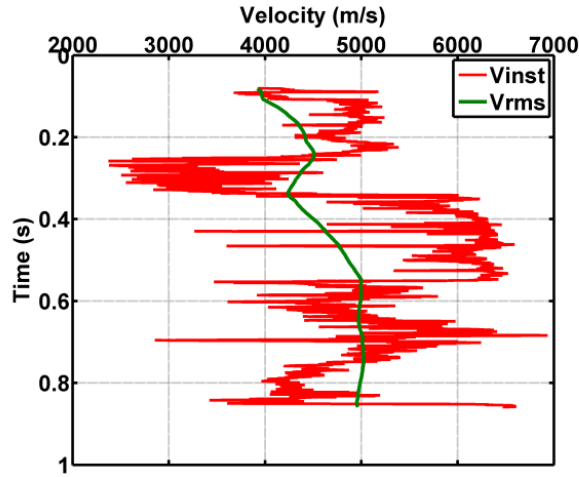


Figure 3.7 – Comparison of the corrected well-logging velocities (red) with the RMS velocities (green) in time domain.

RMS velocities are calculated at different time intervals of 10 millisecond (red), 50 millisecond (green), and 100 millisecond (blue), respectively, as shown in Figure 3.8 (a). Based on the three time intervals, the maximum (V_{max}) and minimum velocities (V_{min}) are calculated as well, as shown in Figure 3.8 (b). When the time interval decreases, the RMS velocities, maximum velocities, and the minimum velocities swing intensively, and the velocities reversal becomes more severe. On the contrary, when the time interval increases, the velocities return to increase with depth.

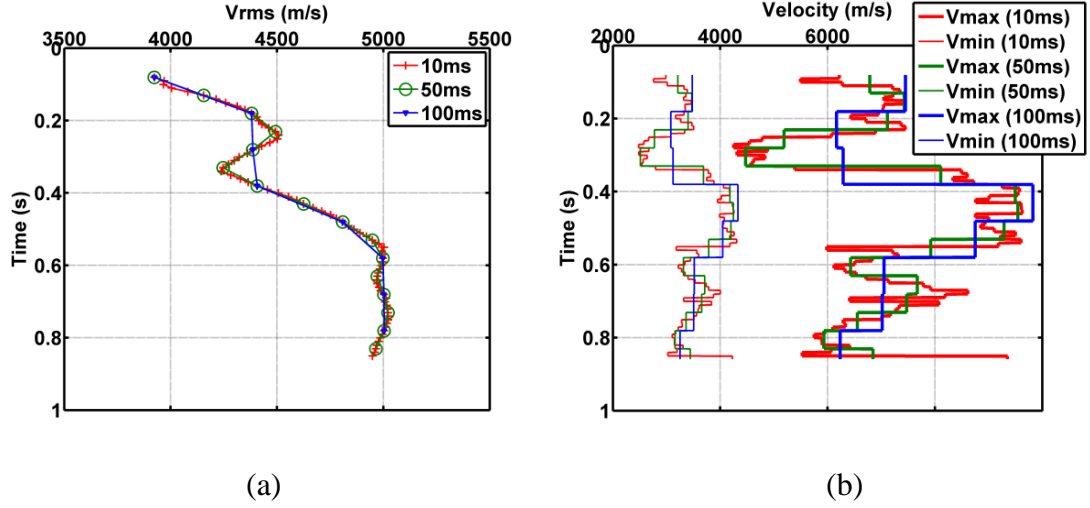


Figure 3.8 – (a) RMS velocities based on different time intervals in time domain, and (b) V_{max} and V_{min} with corresponding time intervals in time domain.

The pore-pressure prediction results according to the different time intervals are shown in Figure 3.9. When the time interval increases, the result swings more intensively.

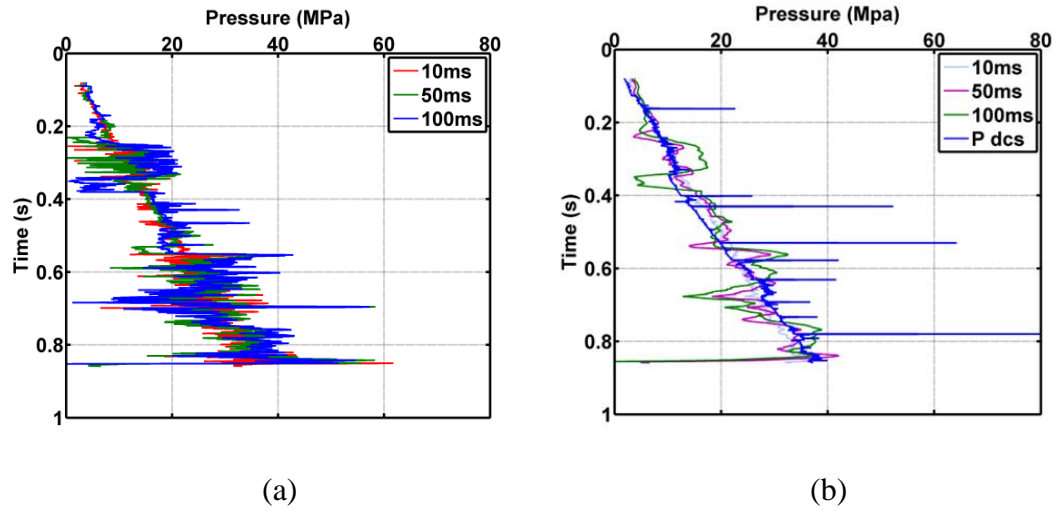


Figure 3.9 – (a) Comparison of the predicted pore-pressure of different time intervals in time domain, and (b) smoothed pressure curves in time domain.

Considering the irrationality of homogeneous stratification based on constant time intervals, the time intervals are divided based on geological information (Figure 3.10).

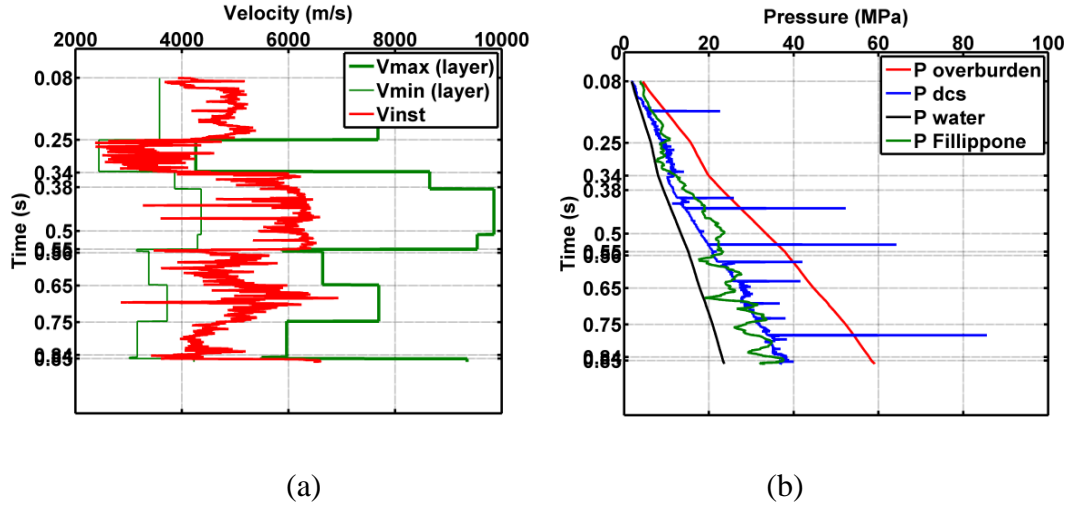


Figure 3.10 – (a) V_{max} (dark green), V_{min} (green), and V_{inst} (red) are estimated based on the layer division of geological information in time domain, and (b) comparison of the predicted pore-pressure (green) with the D exponent pressure (blue) in time domain.

As shown in Figure 3.10, the instantaneous velocities are higher than the maximum velocities at 0.27 s, and this condition could cause a negative pressure value at the corresponding depth, which is not reasonable. The pore-pressure prediction results are much higher than the corresponding D exponent pressure from 0.34 s to 0.50 s, and the pore-pressure prediction results are lower than the corresponding D exponent pressure from 0.60 s to 0.85 s, so the pore-pressure

prediction results do not have a good consistence with D exponent pressure. In other words, the Fillippone approach Test 1 fails to predict a reasonable pore pressure with V_{max} and V_{min} .

3.4.2 The Fillippone approach Test 2

The physical meanings of V_{max} and V_{min} are the seismic velocities of rock skeleton and the formation fluid, respectively. The empirical V_{max} and V_{min} can be selected based on the regional geophysical data and the well-logging data. That is:

$$V_{max} = 2V_{inst}, \quad (3.12)$$

$$V_{min} = 1600m/s. \quad (3.13)$$

This calculation approach is not related to the RMS velocity, so the V_{max} and V_{min} can be directly calculated in the depth domain shown in Figure 3.11 (a). Figure 3.11 (b) shows the comparison of the predicted pore pressure with the D exponent pressure.

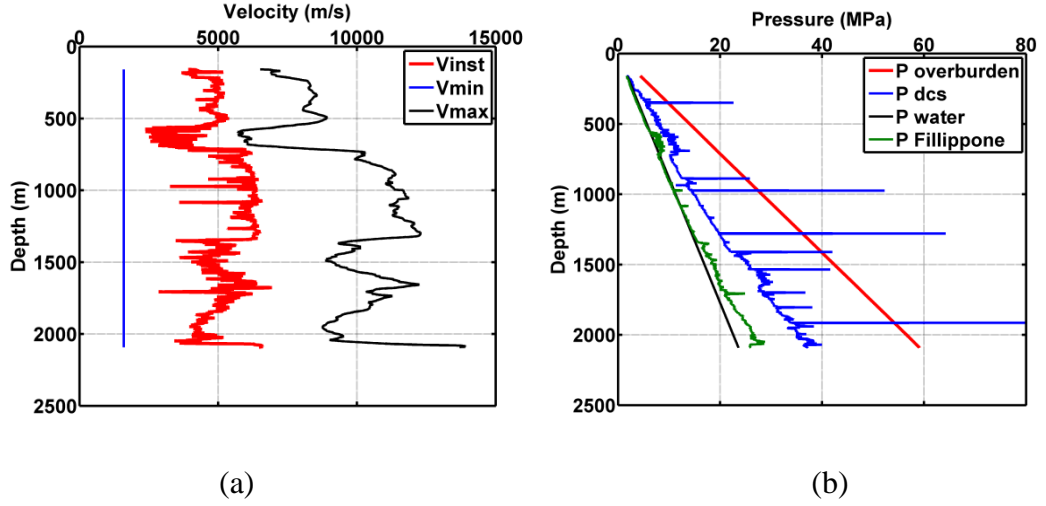


Figure 3.11 – (a) V_{max} (black), V_{min} (blue), and V_{inst} (red) are estimated based on the empirical parameters in depth domain, and (b) comparison of the predicted pore-pressure (green) with the D exponent pressure (blue) in depth domain.

To correct the estimated pressure in Figure 3.11 (b), the pore-pressure slope correction should be conducted with the following formula:

$$P_{slope\ correct} = A \times P_{predict}, \quad (3.14)$$

where, $P_{slope\ correct}$ is the pore-pressure after the slope corrections, A is the correction parameter, and $P_{predict}$ is the pore-pressure prediction result. The correction parameter $A = 1.2215$, which is calculated from the predicted pressure.

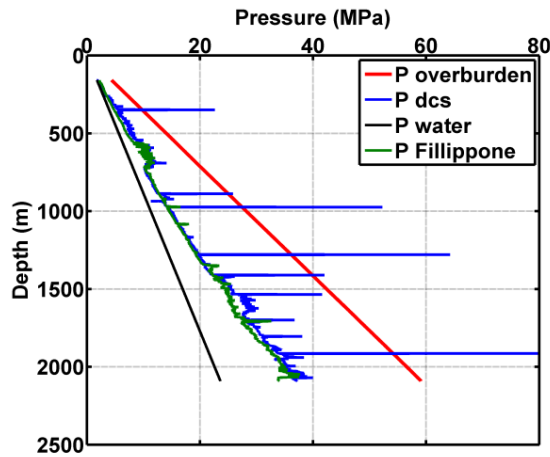


Figure 3.12 – Comparison of the predicted pore-pressure (green) after slope corrections with the D exponent pressure (blue) in depth domain.

As show in Figure 3.12, there is a little difference between two pressure values estimated by D exponent and the Fillippone approach, although the predicted pore pressure are slightly lower than the D exponent pressure values at depth from 1500 m to 1700 m. This test shows that the pore-pressure prediction results based on the selected empirical parameters have a good consistence with D exponent pressure, i.e. The Fillippone approach test 2 makes the pore-pressure prediction results consistent with D exponent pressure. However, this approach lacks the basis of parameters selection and it cannot be applied to the whole study area.

3.4.3 The Fillippone approach Test 3

Test 3 of the Fillippone approach does not depend on the maximum (V_{max}) and minimum velocities (V_{min}) calculation; instead, it calculates the maximum (V_{mxp}) and minimum compaction velocities (V_{mnp}):

$$P_{Fillippone} = P_0 \times \frac{V_{mxp} - V_{in}}{V_{in} - V_{mnp}}, \quad (3.15)$$

where, V_{mxp} and V_{mnp} are the maximum and minimum compaction velocities,

$$\begin{cases} V_{mxp} = 1.4V_0 e^{a_0 T} \\ V_{mnp} = 0.7V_0 e^{0.5a_0 T} \end{cases}, \quad (3.16)$$

where,

$$V_0 = V_Q e^{0.5a_1 T_Q}, \quad (3.17)$$

$$a_1 = e^{\frac{-V_Q}{10^4}}, \quad (3.18)$$

$$a_0 = 0.7e^{\frac{-V_Q}{10^4}}, \quad (3.19)$$

V_Q is the RMS velocity at T_Q , and $T = T_Q$ is the two-way travel time at the calculation point. Figure 3.13 (a) shows the comparison of the maximum (dark green) and minimum compaction velocities (green) with the instantaneous velocities (red). In this calculation approach, the maximum (V_{mxp}) and minimum compaction velocities (V_{mnp}) are not related to the time intervals, and the $V_{in} > V_{mxp}$ condition does not exist. Figure 3.13 (b) gives the comparison between the predicted pore-pressure (green) with the D exponent pressure (blue).

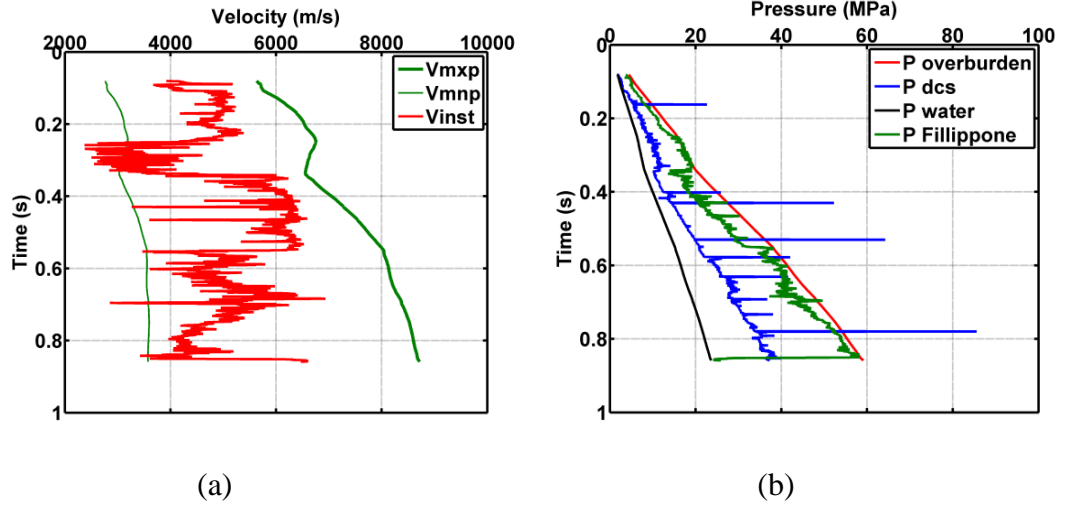


Figure 3.13 – (a) $V_{m xp}$ (dark green), $V_{m np}$ (green), and V_{inst} (red) in time domain, and (b) comparison of the predicted pore-pressure with the D exponent pressure in time domain.

There are two commonly-used Fillippone correction formulas to improve the matching of the pore-pressure prediction results with the D exponent pressure (Yun, 1996). One is:

$$P_{Fillippone} = F_{V_{in}} \times P_0 \times \frac{V_{m xp} - V_{in}}{V_{in} - V_{m np}}, \quad (3.20)$$

where,

$$F_{V_{in}} = A e^{B V_{in}}, \quad (3.21)$$

A and B are the correction parameters. The correction parameter $A = 0.4845$, $B = 0.000063$, which are calculated from the D exponent pressure. The other Fillippone correction formula is (Ma, 2012):

$$P_{Fillippone} = P_0 \times \left(\frac{V_{m xp} - V_{in}}{V_{in} - V_{m np}} \right)^n, \quad (3.22)$$

where, n is the correction parameter. The correction parameter n is calculated from the

D exponent pressure. The value of n is 0.2393 in this study.

Figure 3.14 shows the comparison of the predicted pore-pressure after corrections and the D exponent pressure.

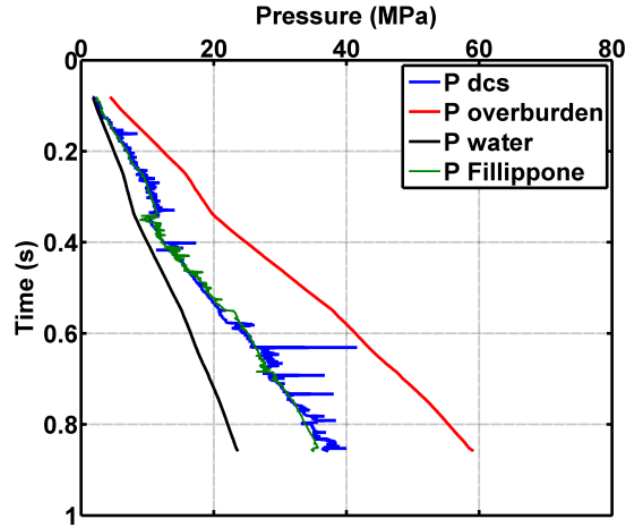


Figure 3.14 – Comparison of the predicted pore-pressure (green) after corrections with the D exponent pressure in time domain (blue).

In Figure 3.14, the predicted pore-pressure has a reasonable matching with D exponent pressure, so the result based on the Fillippone approach Test 3 is reasonable. This approach avoids the time intervals stratification and only depends on the RMS velocity and two-way travel time. This gives rise to a significant improvement comparing with Test 1 and Test 2. However, the three correction parameters (A , B , and n) should be derived from the real pressure measurements. In order to simplify the computation procedure, another pore-pressure prediction approach, i.e. the Eaton approach, is considered.

3.5 The Eaton approach

3.5.1 Basic principle

In the original Eaton's formula, transit time is used, and it can be derived to be a function of the seismic interval velocity (Chilingar et al., 2002):

$$P_{Eaton} = P_0 - (P_0 - P_h) \times \left(\frac{V_{inst}}{V_{normal}} \right)^N, \quad (3.23)$$

where, P_{Eaton} is the predicted pore pressure, P_h is the normal hydrostatic pressure, V_{inst} is the instantaneous velocity of the observed shale, V_{normal} is the seismic velocity for normal compaction, and N is an empirical coefficient related to the location characteristics (a typical N value in the Gulf of Mexico is 3). The empirical coefficient $N = 0.33$, which is calculated from the D exponent pressure.

The Eaton approach for pore-pressure prediction can be expressed by following formula:

$$Pressure_{pore} = Overburden\ stress - Effective\ stress. \quad (3.24)$$

Figure 3.15 shows the pore pressure, overburden stress, and effective stress in a borehole.

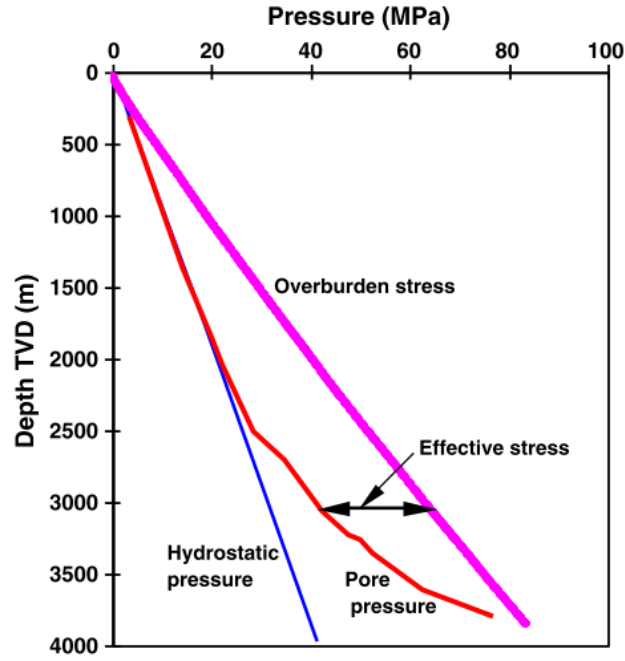


Figure 3.15 – Hydrostatic pressure, pore pressure, overburden stress, and effective stress in a borehole (Zhang, 2011).

The Eaton's formula is based upon the assumption of sediment compaction; thus, it is appropriate in sand-shale sequences only (Chilingar et al., 2002). When $V_{inst} = V_{normal}$, the formation is normally compacted, and the effective stress is:

$$\sigma = P_0 - P_w, \quad (3.25)$$

where, P_w is the hydrostatic pressure, and P_0 is the overburden pressure.

Under the normal compaction, the seismic interval velocity increases with increasing depth for sand and shale formations.

There are two normal compaction velocity calculation approaches. The first one is a linear normal compaction velocity calculation approach (Slotnick, 1936):

$$V_{normal} = V_0 + B \times Depth, \quad (3.26)$$

where, V_0 is the intercept (velocity at surface) and B is a parameter. For this study, the intercept V_0 is 5200 m/s and the parameter B is calculated to be 0.5 based on the analysis of D exponent.

Hottmann and Jahnsen (1965) introduced an exponential normal compaction velocity calculation approach:

$$\ln\left(\frac{1}{V_{normal}}\right) = \ln\left(\frac{1}{V_0}\right) + B \times Depth, \quad (3.27)$$

where, V_0 is the intercept and B is a parameter. The intercept V_0 is 5000 m/s and the parameter B is calculated to be - 0.0001 based on the analysis of D exponent.

Those approaches rely on normal compaction trend (NCT) analysis of seismic velocity versus depth, and then use the velocity deviation from the NCT as a measurement of pore pressure, employing calibration functions (Dutta, 2002). The essential steps are defined as follows:

- The normal compaction trend should be established from mudstone (pick normal compaction sample points in the pure and thick mudstone). The basic principle is that the mudstone porosity is stable, and any changes of mudstone porosity could cause abnormal pressure;
- One or more normal compaction velocity can be established based on the regional geological sedimentary history. Other wells' normal compaction velocities in the same area can be used as reference;
- Construct a normal compaction trend line for the area under investigation and overlay this trend line on top of seismically derived acoustic log;

- Normal compaction trend denotes a depth versus velocity relationship for a rock which has compacted under hydrostatic pressure conditions;
- Any attempt to derive a normal compaction trend line, by fitting a couple of pressure measurements, must be viewed with considerable skepticism;
- Such trend lines are likely to vary from well to well, even in the same mini-basin with the same geology and rocks.

3.5.2 Test of the Eaton approach

Due to the absence of thick mudstone formations in Well A, the normal compaction trend line cannot be established. So in this test, the normal compaction trend line is derived from the D exponent pressure. The normal compaction velocity results in linear condition as show in Figure 3.16.

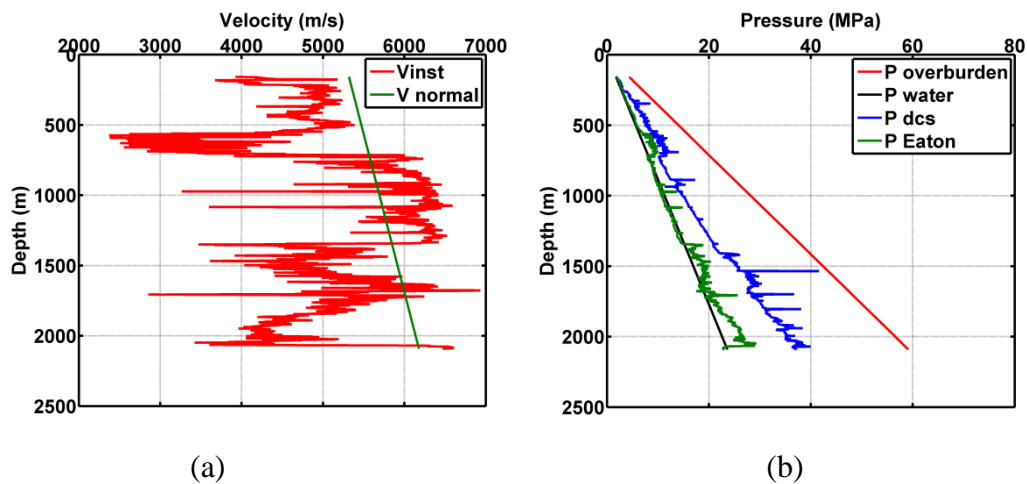


Figure 3.16 – (a) Comparison of the normal compaction velocities (green) with the instantaneous velocities (red) in depth domain, and (b) comparison of the predicted pore-pressure (green) with the D exponent pressure (blue) in depth domain.

To improve the matching of the predicted pore pressure and the D exponent pressure, the slope of the pore-pressure curve has to be corrected as shown in Figure 3.17 (corrected by the formula 3.14). The correction parameter A is 1.2167, which is calculated from the predicted pore pressure.

In Figure 3.17, the pore-pressure prediction results in target formation from 1859 m to 2055 m have a good consistence with the D exponent pressure.

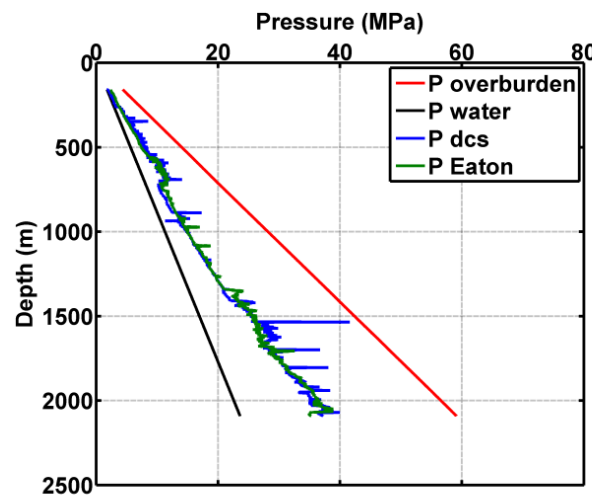


Figure 3.17 – Comparison of the predicted pore pressures (green) after slope corrections with the D exponent pressure (blue) in depth domain.

The normal compaction velocities estimated by the exponential approach is shown in Figure 3.18.

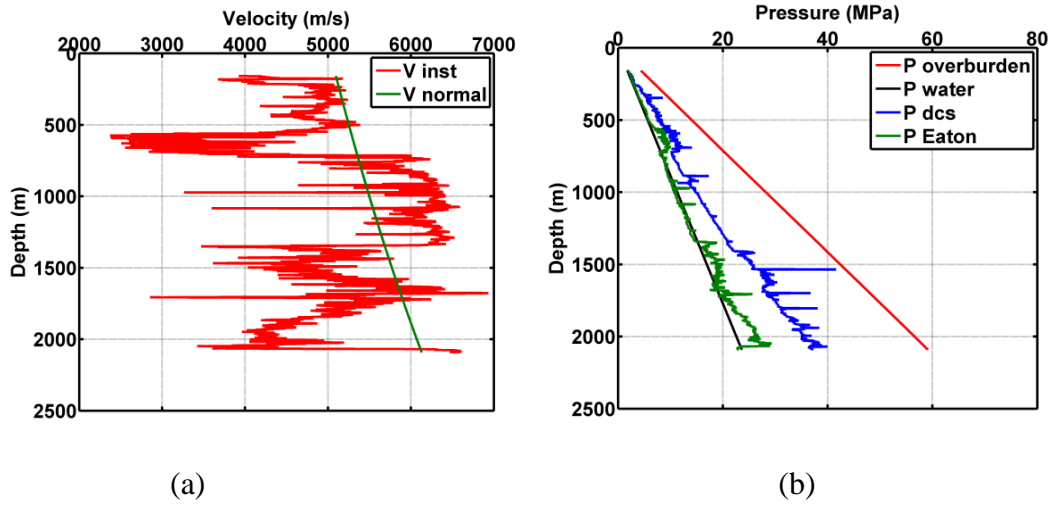


Figure 3.18 – (a) Comparison of the normal compaction velocities (green) with the instantaneous velocities (red) in depth domain, and (b) comparison of the predicted pore pressure (green) with the D exponent pressure (blue) in depth domain.

The pore-pressure curve slope has to be corrected in Figure 3.19 (corrected by the formula 3.14). The correction parameter A is 1.1278, which is calculated from the predicted pressure.

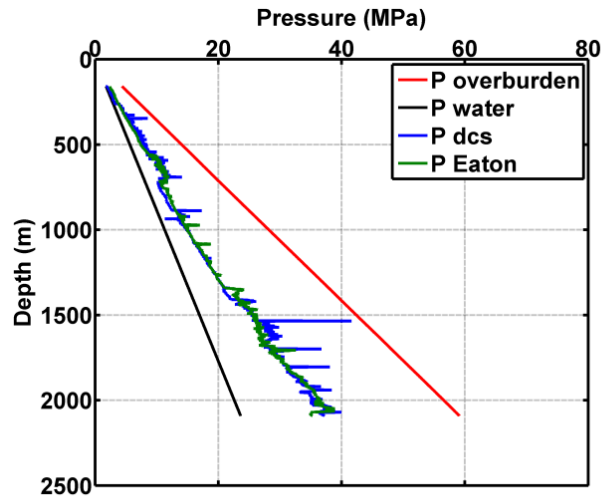


Figure 3.19 – Comparison of the predicted pore pressures (green) after slope corrections with the D exponent pressure (blue) in depth domain.

In the target formation, from 1859 m to 2055 m, the pore-pressure prediction results have a good consistence with D exponent pressure.

In the Eaton approach, the normal compaction trend line is established in the thick, homogenous mudstone intervals, but Well A only has three thin mudstone intervals (see Table 1.3). Hence, the two approaches discussed above, namely, Fillippone and Eaton, were used together to establish a new normal compaction velocity calculation approach.

3.5.3 The Fillippone + Eaton approach

3.5.3.1 The Fillippone + Eaton approach 1

In order to establish a reasonable normal compaction trend line in Well A, the maximum (V_{mxp}) and minimum compaction velocities (V_{mnp}) from the Fillippone approach are used in following tests.

The first test is based on the normal compaction velocity is an average value between maximum and minimum compaction velocities:

$$V_{normal+Fillippone}^2 = \frac{V_{mxp}^2 + V_{mnp}^2}{2}, \quad (3.28)$$

where, $V_{normal+Fillippone}$ is the normal compaction velocity, V_{mxp} is the maximum compaction velocity, and V_{mnp} is the minimum compaction velocity.

This normal compaction velocity calculation approach does not depend on the time interval stratification, but on the RMS velocity only. The comparison of the maximum (V_{mxp}), minimum (V_{mnp}), normal compaction velocities ($V_{normal+Fillippone}$), and the instantaneous velocities (V_{inst}) are shown in Figure 3.20. The pore-pressure can be calculated by the Eaton formula (formula 3.23). The pore-pressure prediction results based on this approach is show in Figure 3.21.

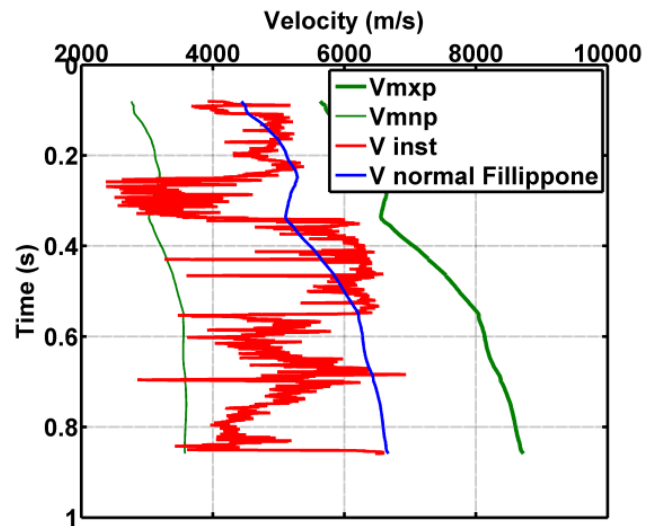


Figure 3.20 – $V_{m xp}$ (dark green), $V_{m np}$ (green), V_{normal} (blue), and V_{inst} (red) in time domain.

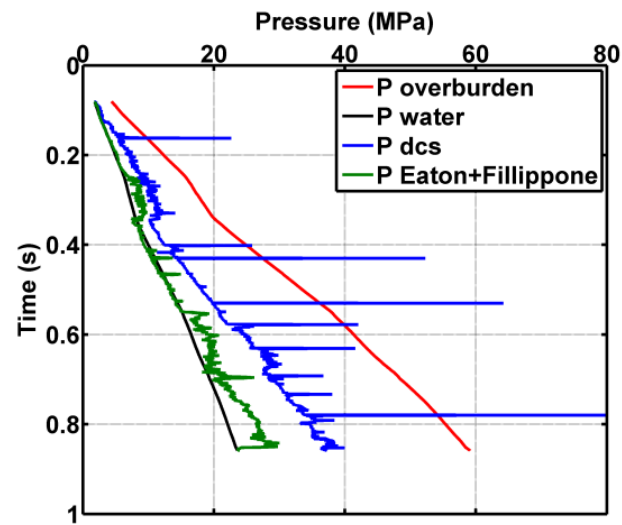


Figure 3.21— Comparison of the predicted pore pressure (green) with the D exponent pressure (blue) in time domain.

The predicted pore-pressure curve slope has to be corrected (corrected by the formula 3.14), as shown in Figure 3.22. In our case the correction parameter A is 1.3214, which is calculated from the predicted pressure.

In Figure 3.22, the pore-pressure prediction results in target formation, from 0.75 s to 0.90 s, have a good consistence with the D exponent pressure, but this approach is lack of establishment basis, another approach is considered.

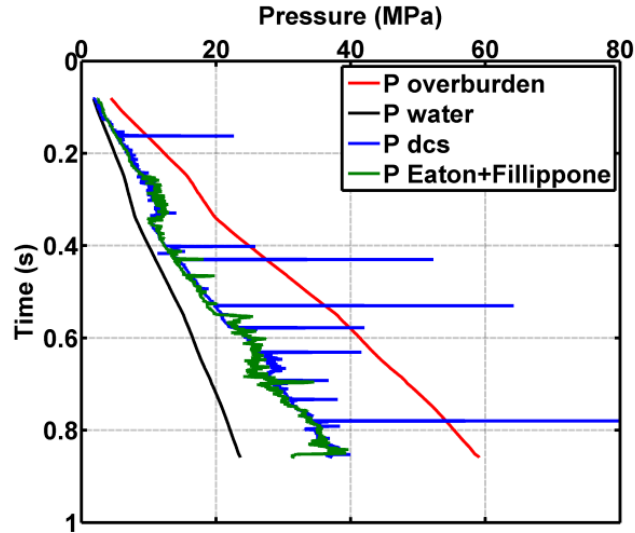


Figure 3.22 – Comparison of the predicted pore-pressure (green) after slope corrections with the D exponent pressure (blue) in time domain.

3.5.3.2 The Fillippone + Eaton approach 2

Assume the formation is normally compacted, then:

$$P_{Eaton} = P_{Fillippone}, \quad (3.29)$$

where, P_{Eaton} is the predicted pore pressure based on the Eaton formula (formula 3.23) and $P_{Fillippone}$ is the predicted pore pressure based on the Fillippone formula (formula 3.15),

when $V_{inst} = V_{normal}$,

$$P_0 - (P_0 - P_w) = P_0 \times \frac{V_{mxp} - V_{normal}}{V_{mxp} - V_{mnp}}, \quad (3.30)$$

where, P_0 is the overburden pressure, P_w is the hydrostatic pressure, V_{mxp} is the maximum compaction velocity, V_{mnp} is the minimum compaction velocity, V_{inst} is the instantaneous velocity, and V_{normal} is the normal compaction velocity.

The normal compaction velocity $V_{normal+Eaton}$ can be calculated by:

$$V_{normal+Eaton} = V_{mxp} - \frac{P_w}{P_0} (V_{mxp} - V_{mnp}), \quad (3.31)$$

where, P_0 is the overburden pressure, P_w is the hydrostatic pressure, V_{mxp} is the maximum compaction velocity, and V_{mnp} is the minimum compaction velocity. The pore-pressure can be calculated by the Eaton formula (formula 3.23).

Figure 3.23 shows the seismic velocities for normally compacted condition, which are calculated based on these two Fillippone + Eaton approaches, and show good coherence with each other.

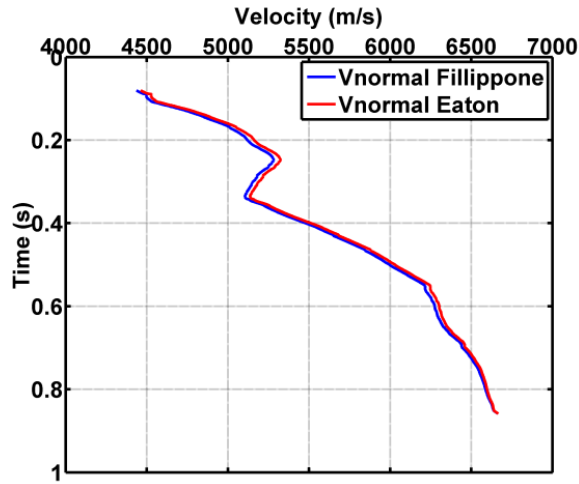


Figure 3.23 – Comparison of the normal compaction velocities based on two approaches in time domain.

The comparison of the predicted pore pressure based on the Fillippone + Eaton approach 2 with the D exponent pressure is shown in Figure 3.24.

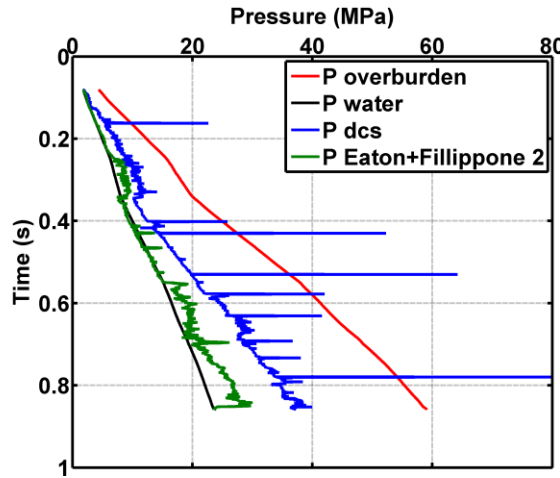


Figure 3.24 — Comparison of the predicted pore pressure (green) based on the Fillippone + Eaton approach 2 with the D exponent pressure (blue) in time domain.

To further improve the predicted pore pressure, the predicted pore-pressure curve slope has to be corrected (corrected by the formula 3.14). Figure 3.25 shows the corrected pore-pressure curve using the correction parameter $A = 1.3308$. In Figure 3.25, the pore-pressure prediction result shows that the target formation from 0.75 s to 0.90 s is consistent with the D exponent pressure. The Fillippone + Eaton approach 2 is applied in the 3D pore-pressure prediction in the target formation.

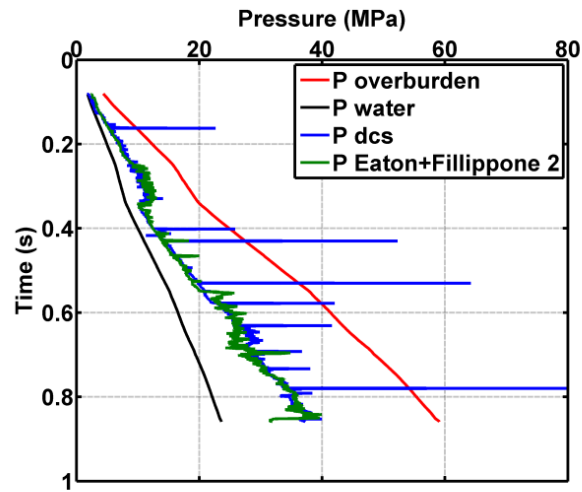


Figure 3.25 – Comparison of the predicted pore pressure (green) after slope corrections with the D exponent pressure (blue) in time domain.

Chapter 4

Pore-pressure prediction in the target formation

4.1 Model-based inversion

Seismic inversion constructs the underground geological information based on seismic data. A challenge to all inversion is non-uniqueness; in other words, multiple geological models could match with the given data. In order to improve the accuracy of inversion result, additional geophysical data should be involved as constraints. Therefore, well-logging stratification data with velocity spectrum are used to establish a low frequency velocity background, and set up an initial model for the seismic inversion.

Figure 4.1 shows a model-based inversion flowchart used in this study. The constraint of this inversion result is the acoustic velocity from well-logging.

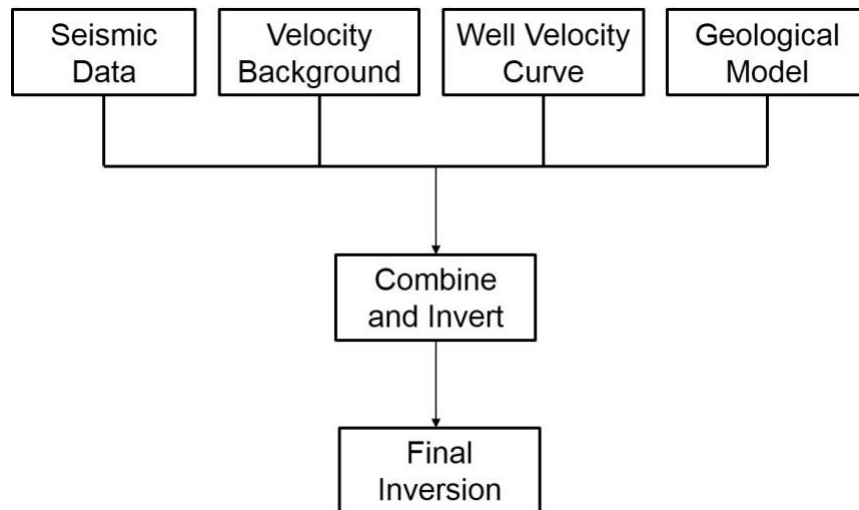


Figure 4.1 – Model-based inversion flowchart.

Main steps of model-based inversion:

- Major intervals tracing and well-logging data calibration with seismic data;
- Wavelet extraction by using acoustic logging curve;
- Model building based on acoustic logging curve and RMS velocity;
- Inversion iteration based on the model and obtains impedance inversion result;
- Conversion of impedance into velocity and density.

4.2 3D pore-pressure prediction in the target formation

The velocity and density inversion results are converted from the impedance inversion result using the Strata software.

The initial model of inversion is given in Figure 4.2.

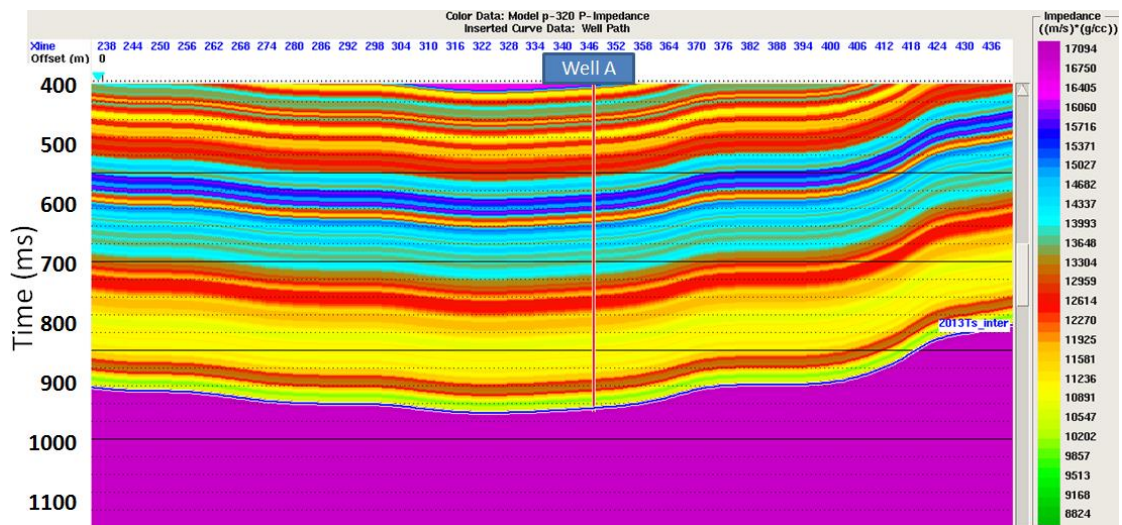


Figure 4.2 – Initial model for velocity inversion in time domain.

Figure 4.3 shows the result of impedance inversion.

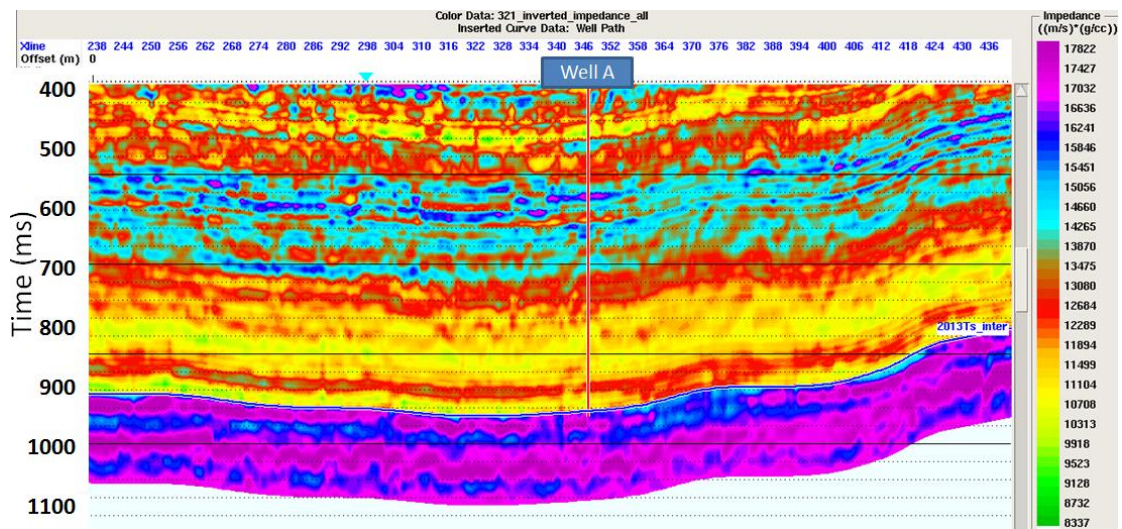


Figure 4.3 – Impedance inversion results in time domain.

The impedance inversion results are then converted into seismic velocity and density, as shown in Figure 4.4 and Figure 4.5.

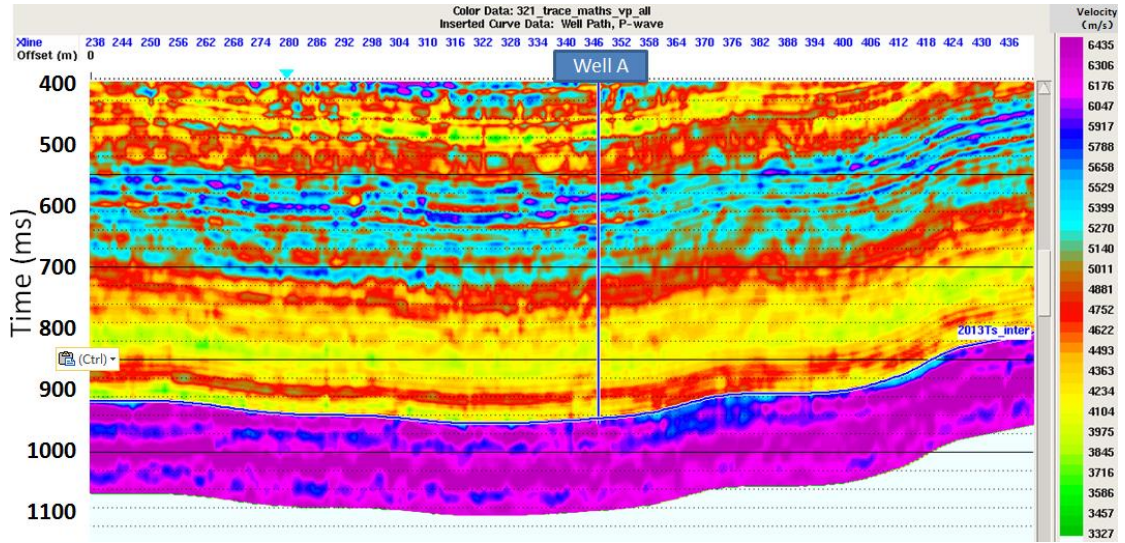


Figure 4.4 – Velocity inversion results in time domain.

In Figure 4.4, the target formation at 950 ms has a relatively lower velocity value compared to the seismic velocities of the surrounding formations. This phenomenon could be the results of the high-pressure caused by the accumulation of shale gas. In shallower depth, from 600 ms to 700 ms, there is a relatively high interval velocity. By comparing with well-logging data at the same time, we suspect that this is caused by the variations in the lithology in that formation, which is composed basalt with high velocity characteristics.

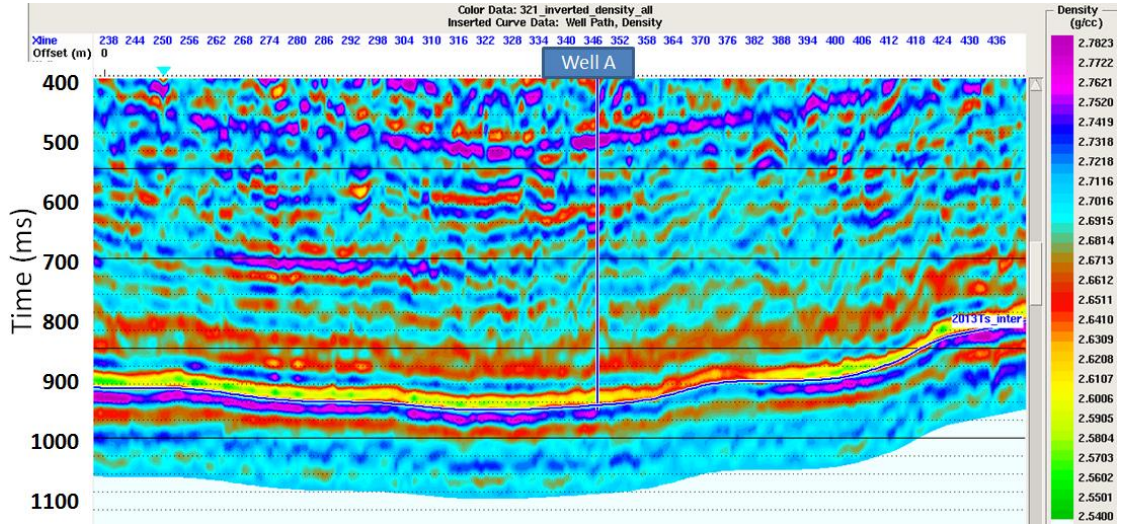


Figure 4.5 – Density inversion results in time domain.

The new normal compaction velocity calculation approach (the Fillippone + Eaton approach 2) is applied in the 3D pore-pressure prediction in the target formation.

The 3D pore-pressure prediction results and the corresponding pressure coefficient results in the study area are shown in Figure 4.6 and Figure 4.7, respectively. The pressure coefficient calculation based on the ratio of the pore pressure with the corresponding time or depth hydrostatic pressure (Chilingar et al., 2002):

$$C_p = \frac{P_{pore}}{P_w}, \quad (4.1)$$

where, C_p is the pressure coefficient, P_{pore} is the predicted pore-pressure, and P_w is the corresponding time or depth hydrostatic pressure.

In Figure 4.6, the 3D pore-pressure prediction results change gently. There isn't an abnormally high-pressure or low-pressure zone. In the shallow depth (0.25 s), there

is a relatively high-pressure zone. This phenomenon results from the stratigraphy consisting of coal seams in that depth, which has a lower velocity value and induces a higher pressure prediction result.

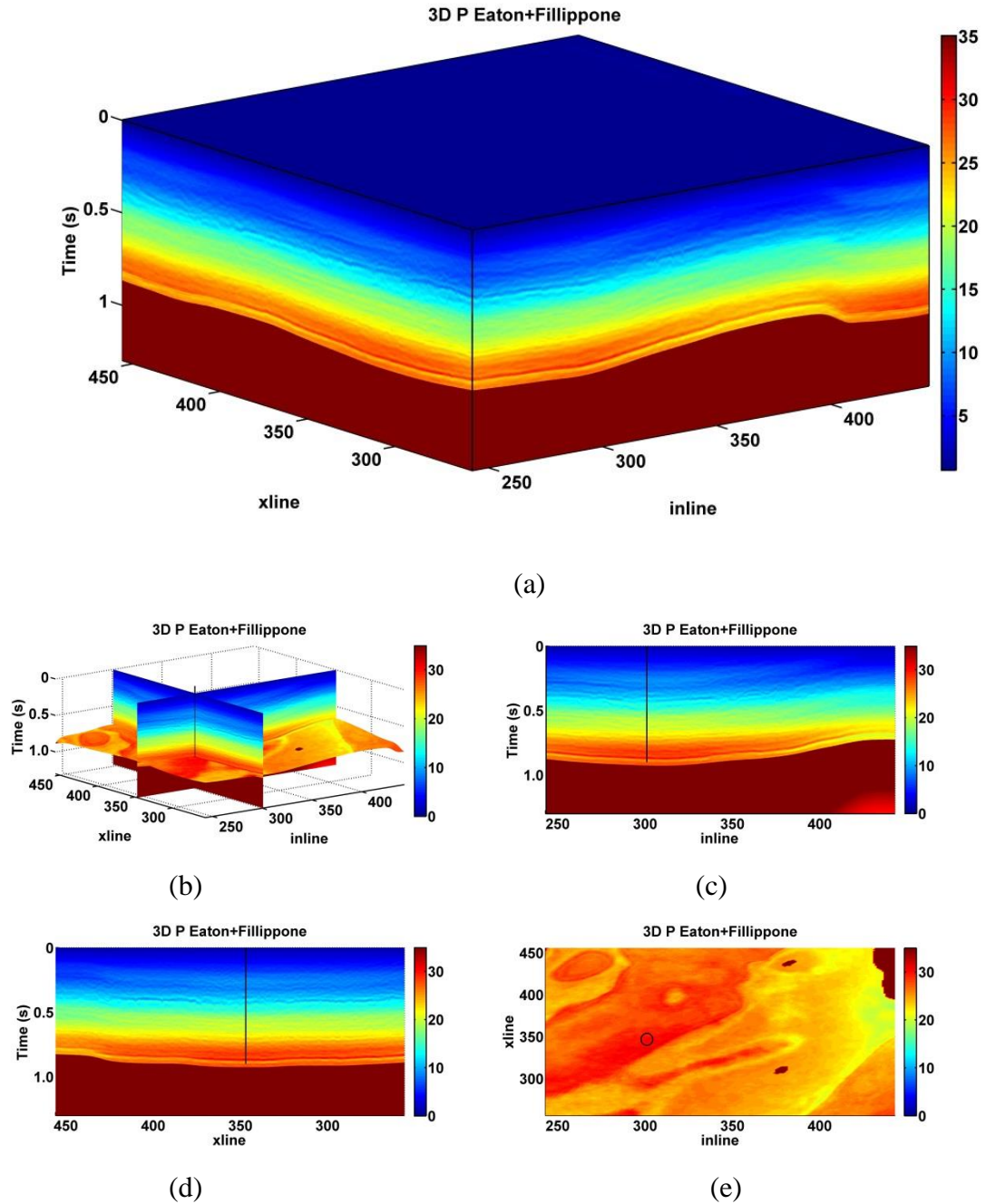


Figure 4.6 – (a) 3D pore-pressure prediction results, (b) inline, xline, and target formation 3D pore-pressure prediction results with Well A, (c) inline cross section profile with Well A, (d) xline cross section profile with Well A, and (e) target formation cross section profile with Well A (unit: MPa).

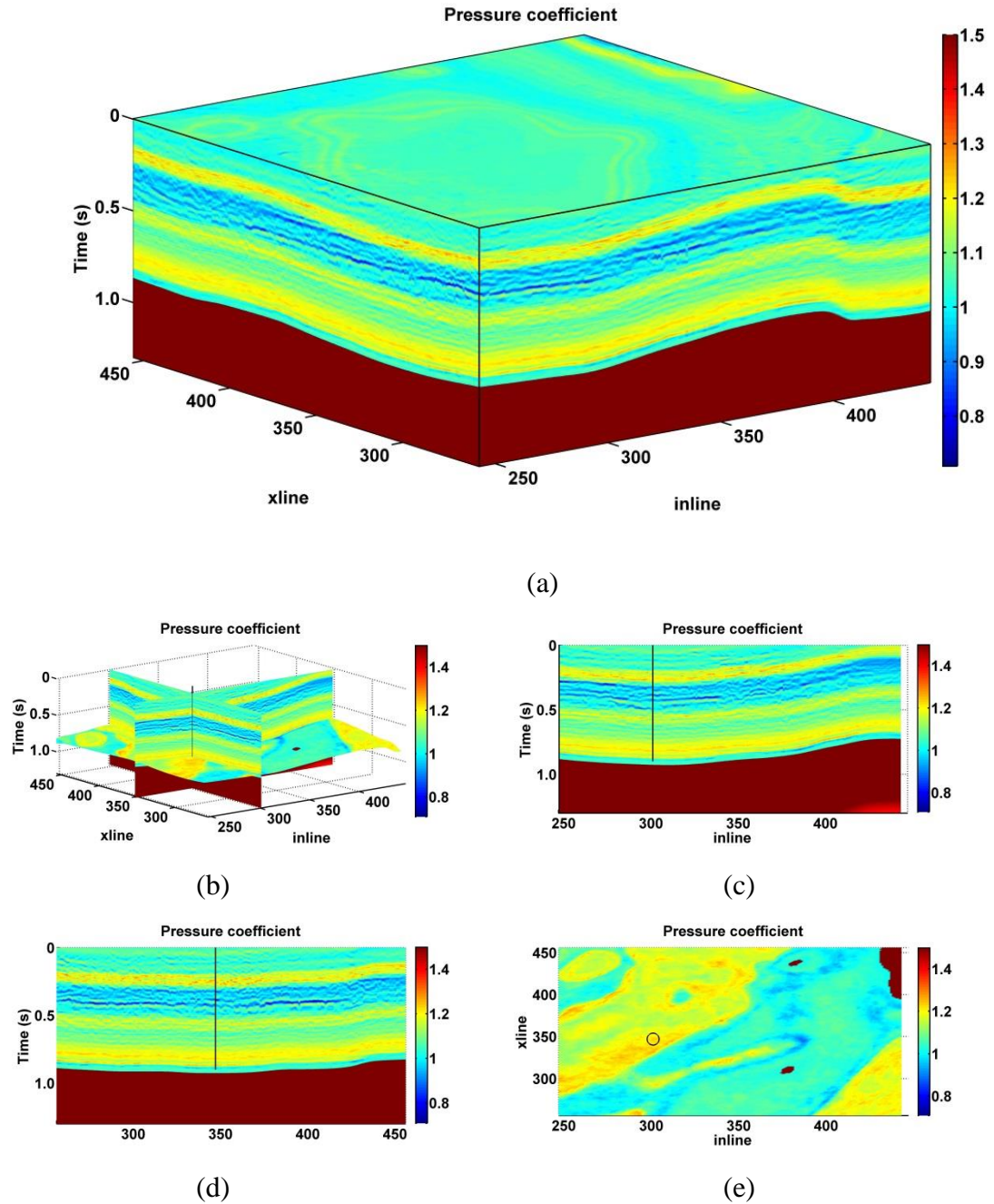


Figure 4.7 – (a) 3D pore-pressure prediction coefficient results, (b) inline, xline, and target formation 3D pore-pressure prediction results with Well A, (c) inline cross section profile with Well A, (d) xline cross section profile with Well A, and (e) target formation cross section profile with Well A.

The predicted pore pressure and the corresponding pressure coefficient are extracted along the target formation shown in Figure 4.8 and Figure 4.9, respectively. Well A is located at a relatively high pressure zone (around 30 Mega Pascal), and the corresponding pressure coefficient is about 1.18. Pressure coefficient of well B is lower than that of Well A. The pore pressure of Well B in the target formation is around 27 Mega Pascal, and its pressure coefficient is about 1.1. In addition, the production capacity of Well A is higher than that of Well B. The target formation velocities are shown in Figure 4.10, and it has an inverse relation with pressure. The velocity value of well B is higher than that of Well A, while the pore-pressure prediction result of Well B is lower than that of Well A.

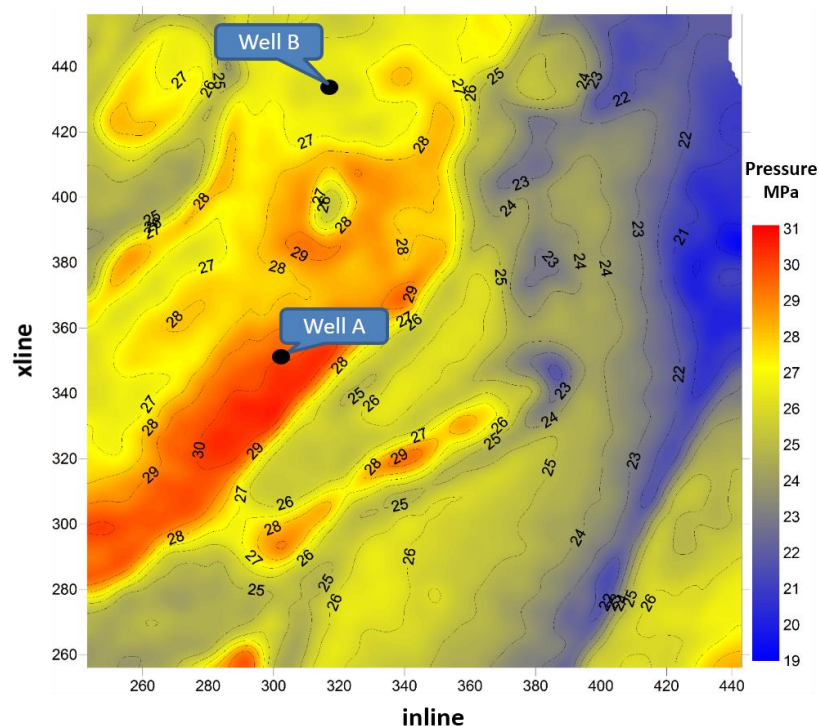


Figure 4.8 – Predicted pore-pressure in the target formation (unit: MPa).

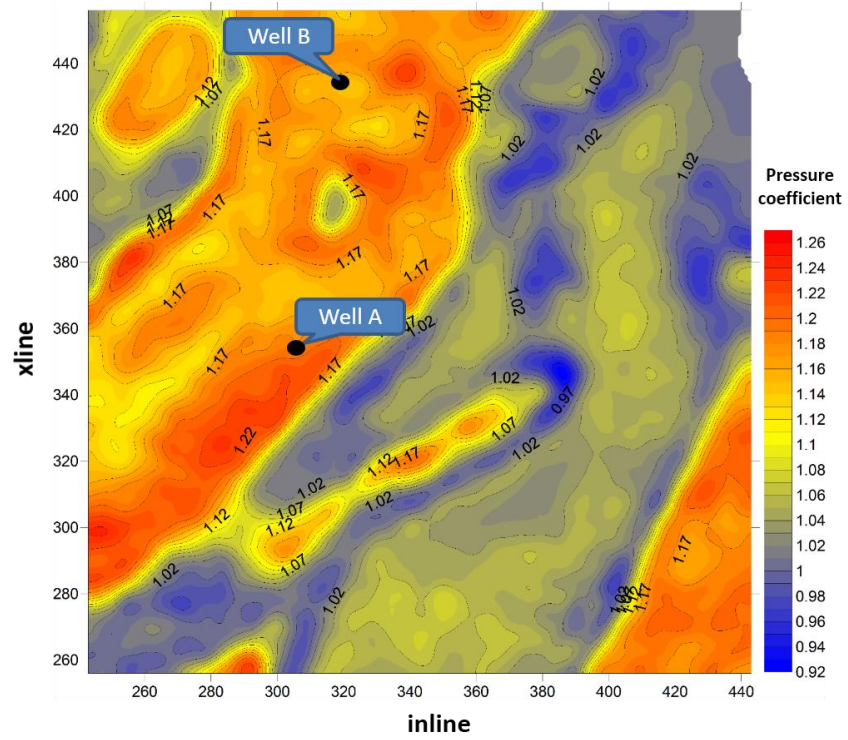


Figure 4.9 – Predicted pore-pressure coefficient results in the target formation.

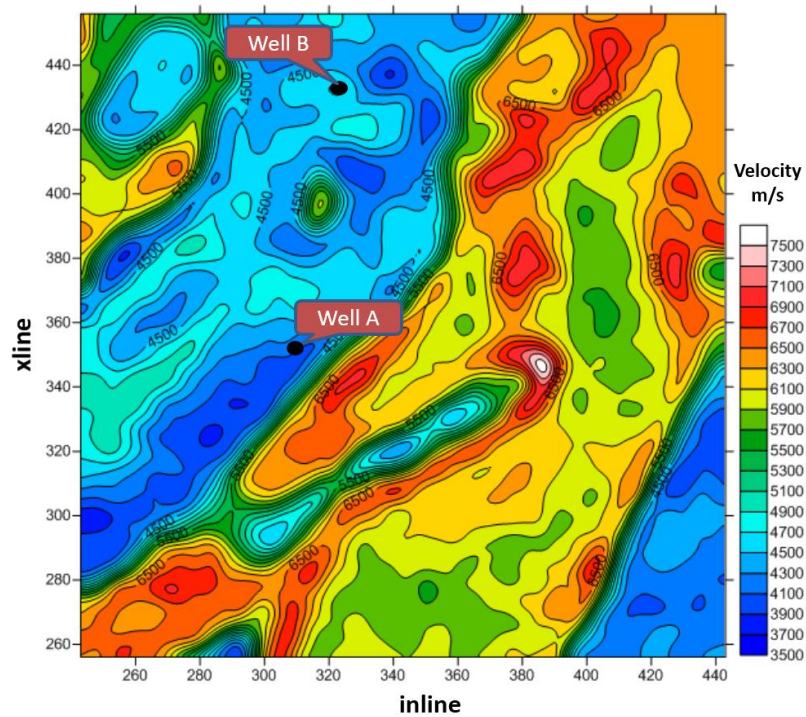


Figure 4.10 – Velocity inversion results in the target formation (unit: m/s).

Due to limited amount of available geophysical data in Well B, such as depths with corresponding pressure coefficients and well-logging velocities data (from 1500 m to 2500 m), this pore-pressure prediction approach can get a reasonable prediction, but it may not be very satisfying. In Figure 4.11, the velocity inversion results (blue) have a reasonable consistence with the well-logging velocity measurements (red) in Well B.

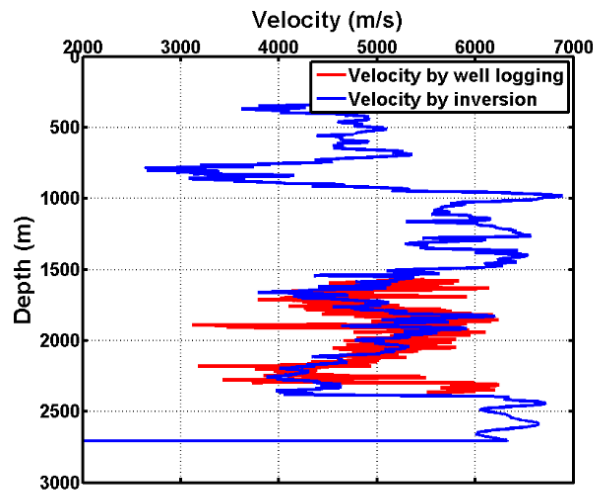


Figure 4.11 – Comparison of the velocity inversion results (blue) with the well-logging velocity measurements (red) for Well B in depth domain.

The comparison of predicted pore-pressure coefficients and the measured pore-pressure coefficient measurements in Well B is shown in Figure 4.12. In the target formation from 1960 m to 2180 m, the pressure coefficient prediction results (green) is within the range between maximum (red) and minimum pressure coefficient measurements (blue).

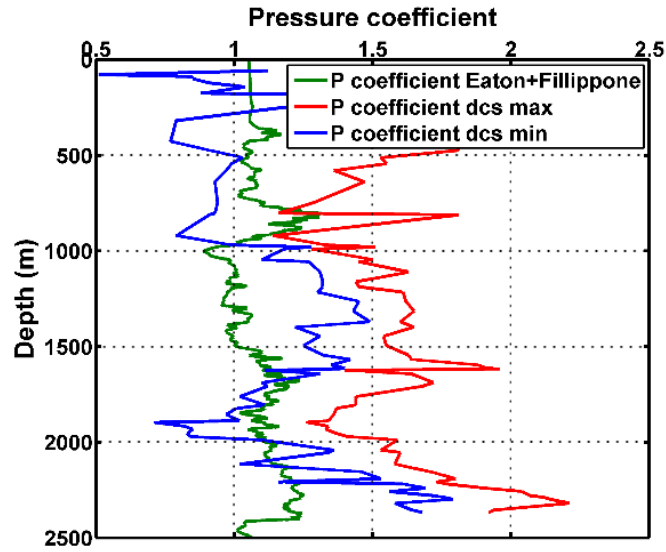


Figure 4.12 – Comparison of the predicted pore-pressure coefficient results with the pressure coefficient measurements for Well B in depth domain.

The Fillippone + Eaton approach 2 is applied in the 3D pore-pressure prediction in the study area and yielded a reasonable result. The predicted pressure coefficients match well with the measured pressure coefficients for Well B in the target formation.

Chapter 5

Conclusions

Accurate prediction of pore-pressure is useful to revealing the enrichment characteristics and passageway of hydrocarbons as well as lithological variation and characteristics of hydrocarbon reservoirs. In the southern Sichuan Basin, China, the potential shale gas reservoirs usually have abnormally high-pressure, so the ability to predict the pore-pressure of the target formation is critical for shale gas exploration.

In this study two empirical approaches of pore-pressure prediction, namely Fillippone and Eaton, have been based the geophysical data of Well A. The Fillippone approach in Test 3 predicts the overpressure based on the RMS velocity and two-way travel time. This predicted result is reasonable with a significant improvement compared to that of the Fillippone Test 1 and Test 2. However, three correction parameters should be fitted for the real measurement. Hence, the Eaton approach was introduced to better fit those parameters. The Eaton approach requires a large number of thick mudstone formations to establish the normal compaction trend line. However, the Well A in this study lacks thick mudstone formations. To overcome the dependence of thick mudstones a new approach of computing seismic velocity for

normal compaction, called “Fillippone + Eaton” normal compaction velocity calculation, was introduced in this study based on the maximum and minimum compaction velocities calculated from the Fillippone formula. This new and easy-to-use approach improves the parameter setting of the two existing approaches, and has the potential to be applied in 3D pore-pressure prediction in the study area.

After model-based inversion, the 3D impedance was converted to velocity and density. The pore-pressure prediction and corresponding pressure coefficient results can be extracted along the target formation. Well A is in a relatively high-pressure zone, and its predicted pressure is higher than the value of Well B, while the velocity value of Well A is lower than Well B. These results are consistent with the field measurement. The predicted pressure coefficient is about 1.11 in the target formation of Well B, which is consistent with pressure coefficient measurement in Well B.

The new approach of “Fillippone + Eaton” for seismic velocity estimation in normal compaction situation is based on the Eaton formula. Its application in the 3D pore-pressure prediction in the study area yielded a reasonable result. Due to limited amount of available geophysical data, the pressure prediction may be over-simplified without considering the complicated lithological condition. Under the other hand, it may help improving the pressure prediction by analyzing the relatively high or low pressure zones in the target formation. Therefore, the pore-pressure prediction results can be used as a reference for potential shale gas reservoir prediction before drilling.

This easy-to-use approach may be applicable in areas where geophysical data are limited.

Chapter 6

Future work

We shall note that only two wells exist in the study area, and there are not enough corresponding geophysical data available. Hence, while the pore-pressure prediction approach appears to be reasonable, it may not satisfy the real condition. In particular, the new normal compaction velocity calculation approach over-simplifies the underground complexity in lithology conditions due to the lack of pure and thick mudstone in Well A. An Eaton formula parameter n is fitted with the D exponent pressure, which is related to specific formation characteristics, and cannot be applied in other areas. With the development of shale gas industry, there will be more wells and geophysical data obtained in the study area, where the normal compaction velocity calculation approach and the Eaton formula parameter calculation should be reconsidered.

References

- Bowers, G. L., 2002, Detecting high overpressure: The Leading Edge, **21**, 174-177.
- Chilingar, G. V., Robertson, J. O., and Serebryakov, V. A., 2002, Origin and prediction of abnormal formation pressures. Development in Petroleum Science, Elsevier Scientific Publishing Company, Amsterdam, Oxford, New York, 21-30, 170-175.
- Chen, S., Zhu, Y., Wang, H., Liu, H., Wei, W., and Fang, J., 2011, Shale gas reservoir characterization: A typical case in the southern Sichuan Basin of China: Energy, **36**, 6609-6616.
- Chopra, C., and Huffman, A., 2006, Velocity determination for pore-pressure prediction: The Leading Edge, **25**, 1502-1515.
- Dutta, N.C., 2002, Geopressure prediction using seismic data: Current status and the road ahead: Geophysics, **67**, 2012–2041.
- Eaton, B.A., 1976, Graphical method predicts geopressure worldwide: World Oil, **183**, 51-56.
- Fillippone, W. R., 1979, On the prediction of abnormally pressured sedimentary rocks from seismic data: Offshore Technology Conference, 3662, 2667-2669.

- Fillippone, W.R., 1982, Estimation of formation parameters and the prediction of overpressures from seismic data: SEG research symposium on geopressure studies, 17-21.
- Gardner, G. H. G., Gardner, L. W., and Gregory, A. R., 1974, Formation velocity and density – the diagnostic basis for stratigraphic traps: *Geophysics*, **6**, 2085–2095.
- Hottman, C.E., and Johnson, R.K., 1965, Estimation of formation pressures from log-derived shale properties: *Journal of Petroleum Technology*, **17**, 717-722.
- Jiang, Z., Guo, L., and Liang, C., 2013, Lithofacies and sedimentary characteristics of the Silurian Longmaxi Shale in the southeastern Sichuan Basin, China: *Journal of Paleogeography*, **2**, 238-251.
- Jorden, J. R., and Shirley, O. J., 1966, Application of drilling performance data to overpressure detection: *Journal of Petroleum Technology*, **18**, 1387-1394.
- Lane, R.A., and Macpherson, L.A., 1976, A review of geopressure evaluation from well logs - Louisiana Gulf Coast: *Journal of Petroleum Technology*, **28**, 963-971.
- Ma, H., 2012, Pore pressure prediction with seismic interval velocity by the modified Fillippone method: *Petroleum Drilling Techniques*, **40**, 56-61.
- Martinez, R. D., Schroeder, J. D., and King, G. A., 1987, Formation pressure prediction using seismic data from the Gulf of Mexico: *Offshore Technology Conference*, 259-268.
- Noah, A.Z., 2013, Pore pressure evaluation from well logging and drilling exponent a Amal field, Gulf of Suez area, Egypt: *Life Science Journal*, **10**, 2889-2898.

- Sayers, C.M., Johnson, G. M., and Denyer, G., 2002, Predrill pore-pressure prediction using seismic data: *Geophysics*, **67**, 1286-1292.
- Slotnick, M. M., 1936, On seismic computation with applications: *Geophysics*, **1**, 9-22.
- Swarbrick, R. E., and Osborne, M. J., 1998, Mechanisms that generate abnormal pressure: an overview: *Bulletin of the AAPG*, **81**, 1023-1041.
- Terzaghi, K., 1943, *Theoretical Soil Mechanics*: Wiley, J. and Sons, Inc.
- Yun, M. H., 1996, Formation pressure prediction using seismic data: *Petroleum Geophysics*, **31**, 575-586.
- Zhang, J., 2011, Pore pressure prediction from well logs: methods, modification, and new approaches: *Earth-Science Review*, **108**, 50–63.
- Zhang, J., 2013, Effective stress, porosity, velocity and abnormal pore pressure prediction accounting for compaction disequilibrium and unloading: *Marine and Petroleum Geology*, **45**, 2-11.